PHYSICAL REVIEW C, VOLUME 60, 044605

Dynamics of two-neutron transfer reactions with the Borromean nucleus ^{6}He

Yu. Ts. Oganessian and V. I. Zagrebaev*
Flerov Laboratory of Nuclear Reaction, JINR, Dubna, Moscow Region, Russia

J. S. Vaagen
SENTEF, Institute of Physics, University of Bergen, N-5007 Bergen, Norway

(Received 30 March 1999; published 30 August 1999)

Low-energy two-neutron transfer reactions with Borromean nuclei (like ^{6}He) are shown to be an effective instrument for studying both the structure of such nuclei and the dynamics of nuclear reactions with their participation. A four-body model is developed to describe such two-nucleon transfer processes within the distorted-wave Born approximation. A realistic three-body bound-state wave function of ^{6}He is used in the calculations and the role of its spatial localization is thoroughly studied. In particular, it is found that the ‘‘dineutron’’ configuration of the ^{6}He nucleus gives the dominant contribution to the two-neutron transfer cross sections. Detailed analysis of the dynamics of these reactions is carried out and the possibilities of using multineutron transfer reactions for studying the structure of other exotic nuclei, in particular ^{8}He, are discussed. [S0556-2813(99)02009-9]

PACS number(s): 25.60.Je, 24.10.Eq, 25.10.+s

I. INTRODUCTION

During the last few years we have seen an increasing interest in studying the properties of radioactive drip-line nuclei at lower beam energies. The variety of nuclear reaction mechanisms at these energies and a growing availability of theoretical models open for more detailed investigation of both the structure of exotic nuclei, the specific features of nuclear reactions induced by these nuclei, and their interplay. The role of various reactions as ‘‘filters’’ for structural characteristics, is of particular interest. Low-energy transfer reactions could allow us to get spectroscopical characteristics of short-lived nuclei, as has been previously done for stable nuclei. A real ‘‘halo state’’ means not only a peripherally located and spatially extended nucleon wave function but also a large value of its spectroscopic factor, i.e., large overlap with respect to the ground/ (a few low-lying) core states. Note, as a further point of interest, that cosmological reactions of nucleosynthesis, in which nuclei far from the stability line play an important role, also take place at low (in fact, sub-barrier) energies.

Among the halo neutron drip-line nuclei there are the very interesting cases of the so-called Borromean nuclei consisting of an inert core and two valence neutrons which cannot bind to the core separately but only as a pair. It means that there are strong neutron-neutron correlations leading to formation of a two-neutron halo structure observed in ^{6}He, ^{11}Li, and ^{14}Be.

The case of ^{6}He is of special interest both from the experimental and theoretical points of view. The ^{6}He nucleus is notable for its constituents, a ^{4}He core which can be treated as structureless with a great degree of confidence, and two neutrons. Moreover, all potentials in the two-body subchannels are well defined in this case and theoretical predictions made within a three-body model should be rather accurate. In particular, the ‘‘dineutron’’ and ‘‘cigarlike’’ configurations predicted for ^{6}He structure [1], await a clear experimental verification.

The available experimental data have not permitted conclusions about the details of the spatial neutron halo structure in ^{6}He to be drawn. The data on the total reaction cross section and the momentum distributions of α particles and neutrons obtained in fragmentation reactions (see, for example, Ref. [2] and references therein) reflect mainly the long tail of the ^{6}He radial wave function. However, such a conclusion follows even from the fact that the neutron pair in ^{6}He is loosely bound. The study of the ^{6}He β^- decay led the authors of Ref. [3] to suggest a new mechanism for delayed deuteron emission which relies on the large overlap of ^{6}He with the α particle and the ‘‘dineutron.’’

Transfer reactions have historically provided a good tool for studying structural parameters and spectroscopic factors of simple nuclear configurations. Therefore, it appears natural to use such reactions also for testing the ^{6}He internal wave function. Understanding the two-neutron correlations in the ^{6}He nucleus could furthermore allow us to conclude more definitely about the structure of other Borromean nuclei and also about multiple Borromean nuclei such as ^{8}He, ^{10}He, and so on.

The optimal choice of projectile energy depends on the reaction under study. In the case of slow collisions ($\leqslant 5$ MeV/nucleon) a strong channel coupling can significantly complicate the reaction mechanism and prevent the use of direct theoretical models to obtain unambiguous conclusions from the experimental data. For collision energy approaching or even exceeding (in the c.m. frame) the nuclear Fermi energy, the probability of transfer processes becomes less and less. Thus, the energy region of 10–30 MeV/nucleon seems to be favorable to study multineutron transfer reactions induced by neutron-rich nuclei.

New experimental results have recently been obtained at FLNR (Dubna) for two-neutron transfer in collisions of ^{6}He with ^{4}He and ^{1}H targets at beam energy of 151 MeV [4,5].

---

*Electronic address: zagrebaev@flnr.jinr.ru

In the present work we investigate the dynamics and spatial location of these two-neutron transfer reactions and analyze the available experimental data [4,5] with focus on new direct information on the structure of the halo nucleus ^{6}He, in particular, on the role of its dineutron configuration. In Sec. II a four-body reaction approach is described along with all the quantities entering in the model (distorted waves, three-body bound-state wave functions, reaction form factors, and so on). Comparison with experimental data on deuteron transfer in the reaction $^4\mathrm{He}+{}^6\mathrm{Li}\rightarrow{}^6\mathrm{Li}+{}^4\mathrm{He}$ at 166 MeV beam energy is also carried out to show the applicability of the developed model. In Sec. III the dynamics of $2n$ transfer in the reaction $^6\mathrm{He}+{}^4\mathrm{He}\rightarrow{}^4\mathrm{He}+{}^6\mathrm{He}$ is investigated in detail. The reaction $^6\mathrm{He}+{}^1\mathrm{H}\rightarrow{}^4\mathrm{He}+{}^3\mathrm{H}$ is discussed in Sec. IV and collision of $^8\mathrm{He}+{}^4\mathrm{He}$ is discussed in Sec. V. Summary and conclusions are presented in Sec. VI.

II. THE MODEL

In describing reactions with Borromean nuclei (like ^{6}He or ^{11}Li) we may take advantage of their predominant few-body structure, but we still have to consider the combined motion of no less than four particles—target nucleus+projectile consisting of a core and two halo nucleons. We cannot yet solve this Schrödinger equation exactly with realistic two-body interaction potentials. So, we need to use an approximation to calculate, for example, the cross section of a process such as two-neutron transfer. The choice of approximation depends on the incident energy. On one hand, at energies of 20 MeV/nucleon (and higher) the direct reaction mechanisms should dominate for not so heavy nuclei. It means, that a general approximation like the distorted-wave Born approximation (DWBA) (with well-determined initial and final asymptotical states of the system and with realistic interactions between the colliding nuclei) should be applicable in this case. On the other hand, nucleon-nucleon collisions of the core nucleons are not so important in nucleus-nucleus interaction at these energies, and in reactions without target excitations we can treat target nucleus and core of the projectile as inert structureless particles. So, we restrict the number of degrees of freedom by considering a four-body system and restrict the reaction dynamics to the contribution of only a one-step direct reaction mechanism. Even in this case the calculation of the $2n$ transfer cross section remains a very difficult problem.

A. The four-body system

Figure 1 shows the four-body system and all coordinates. In particular, the two-nucleon transfer reaction can be written as

$$1+[2(34)]\rightarrow[1(34)]+2. \tag{1}$$

We treat the target nucleus (1) and the core (2) of the projectile as structureless particles not excited in the reaction. For Borromean nuclei (like ^{6}He or ^{11}Li) just the motion of the two valence nucleons (3 and 4) is of especial interest. We can use this four-body approach for some other projectiles also, such as $^6\mathrm{Li}(=\alpha+p+n)$ or $^{18}\mathrm{O}(={}^{16}\mathrm{O}+n+n)$ and so on. In the entrance channel the coordinate set $(\mathbf{x},\mathbf{y_i},\mathbf{R_i})$ is most convenient because the three-body bound-state wave function of the projectile $[2(3,4)]$—$\Psi_i^{(234)}(\mathbf{x},\mathbf{y_i})$—can be calculated as solution of a three-body Schrödinger equation by expanding over hyperspherical harmonics just in $(\mathbf{x},\mathbf{y})$ Jacobi-type coordinates [1]. In the two-nucleon transfer exit channel, the corresponding coordinate set $(\mathbf{x},\mathbf{y}_f,\mathbf{R}_f)$ will be used to calculate the final bound-state wave function $\Psi_f^{(134)}(\mathbf{x},\mathbf{y}_f)$. Neglecting the difference between neutron and proton masses, we have the following connection between the coordinates in terms of $\mathbf{y}_i$ and $\mathbf{R}_i$:

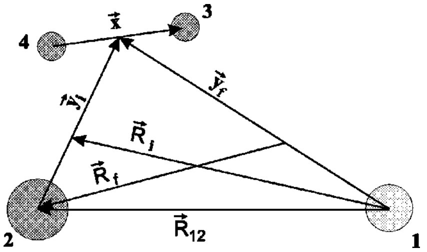

FIG. 1. The coordinate system used in the calculation of the two-nucleon transfer cross section. [2(34)] is the projectile and 1 is the target, 3 and 4 are the transferred nucleons.

$$\mathbf{R}_f=\frac{A_1}{A_1+2}\left[\mathbf{R}_i-\frac{2(A_1+A_2+2)}{A_1(A_2+2)}\mathbf{y}_i\right],$$

$$\mathbf{y}_f=\mathbf{R}_i+\frac{A_2}{A_2+2}\mathbf{y}_i,$$

$$\mathbf{R}_{12}=\mathbf{R}_i-\frac{2}{A_2+2}\mathbf{y}_i. \tag{2}$$

B. Transition amplitude

Assuming that the two-nucleon transfer process at medium and higher energies proceeds mainly by the one-step direct reaction mechanism where the nucleons are transferred simultaneously from the projectile ground state to a final state of the residual nucleus (ejectile), we can write the transition amplitude in standard DWBA form

$$T_{fi}^{\mathrm{DWBA}}(\mathbf{k}_f,\mathbf{k}_i)=\langle\chi_{\mathbf{k}_f}^{(-)}(\mathbf{R}_f)\Psi_f^{(134)}(\mathbf{x},\mathbf{y}_f)|\Delta V|\Psi_i^{(234)}(\mathbf{x},\mathbf{y}_i)\times\chi_{\mathbf{k}_i}^{(+)}(\mathbf{R}_i)\rangle. \tag{3}$$

Here $\chi_{i,f}^{(\pm)}(\mathbf{R}_{i,f})$ are the incoming and outgoing distorted waves calculated with optical model (OM) potentials $U_{i,f}^{\mathrm{OM}}(R_{i,f}),\Psi_{i,f}$ are the three-body bound states of the transferred nucleons (3 and 4) with respect to the inert cores (2 and 1), and the transfer interaction ΔV has one of the following forms (post or prior representation):

$$\Delta V^{\mathrm{post}}=V_{23}(\mathbf{y}_i+\mathbf{x}/2)+V_{24}(\mathbf{y}_i-\mathbf{x}/2)+V_{12}(R_{12})-U_f^{\mathrm{OM}}(R_f), \tag{4}$$

$$\Delta V^{\mathrm{prior}}=V_{13}(\mathbf{y}_f+\mathbf{x}/2)+V_{14}(\mathbf{y}_f-\mathbf{x}/2)+V_{12}(R_{12})-U_i^{\mathrm{OM}}(R_i). \tag{5}$$

This DWBA transition amplitude is a nine-dimensional integral which takes into account the intrinsic three-body motion in the projectile and ejectile and should be evaluated accurately to understand the influence of the internal structure of the loosely bound projectile on the reaction dynamics. Thus, we may be able to obtain directly information concerning the internal structure of Borromean nuclei just from analysis of experimental two-neutron transfer cross sections. We calculate this nine-dimensional integral explicitly (without any essential simplifications) by integrating directly over $\mathbf{x},\mathbf{y}_i$, and $\mathbf{R}_i$, i.e., without partial wave decomposition of the distorted waves and using the full-recoil and finite-range form of the transition amplitude (3). There is some possibility for the halo neutrons to be transferred sequentially, one by one. The DWBA two-step transition amplitude, giving more or less the same angular distribution, is proportional to $\langle \Delta V\rangle/\langle E\rangle$ compared with the amplitude of the direct process [10]. Here $\langle \Delta V\rangle$ is an average transfer interaction while $\langle E\rangle$ is an average energy in the intermediate channels. The amplitudes of direct and sequential mechanisms of $2n$ transfer are comparable with each other in heavy-ion collisions at beam energies of 3–5 MeV/nucleon [10]. But the nature of the Borromean nucleus itself (absence of two-body bound states in ^{5}He or ^{10}Li, and strong neutron-neutron correlations) makes us believe that the simultaneous transfer of both neutrons (neutron pair) is a major part of the two-neutron transfer reactions induced by the Borromean nuclei at beam energies higher than 20 MeV/nucleon.

The differential cross section of the transfer reaction is given as follows:

$$\frac{d\sigma_{fi}}{d\Omega}(E,\theta)=\frac{1}{(2\pi)^2}\,\frac{\mu_i\mu_f}{\hbar^4}\,\frac{k_f}{k_i}\cdot S_f S_i\cdot|T_{fi}(\mathbf{k}_f,\mathbf{k}_i)|^2, \quad (6)$$

where μ_i,μ_f are the reduced masses in the entrance and exit channels, and S_i,S_f are the spectroscopic factors showing the weights of these three-body configurations (i.e., inert core plus two nucleons) in the ground state of the projectile nucleus [2(3,4)] and in the formed state of the ejectile [1(3,4)], correspondingly. For a real halo nucleus this spectroscopic factor should be close to unity. This is a necessary (but not sufficient) condition for formation of the halo structure. Thus, a comparison of the absolute values of the experimental and calculated two-neutron transfer cross sections can already allow us to make a central conclusion: is it possible or not to represent the nucleus under study in the three-cluster form—inert core plus two nucleons? For the ^{6}He nucleus this seems natural due to the compact α-particle core, but for heavier exotic nuclei (even the Borromean ones) it should be tested separately.

More detailed analysis of the angular and energy dependence of the transfer cross section may help us to verify our assumptions about the internal structure of the colliding nuclei, i.e., the spatial structure of the bound-state wave functions $\Psi_{i,f}(\mathbf{x},\mathbf{y})$, and to understand better some specific features of the reaction dynamics with loosely bound nuclei.

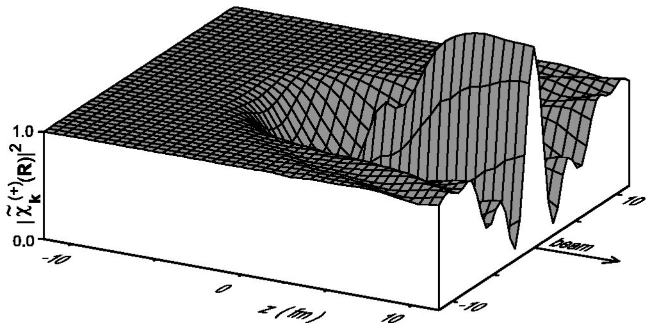

FIG. 2. The wave-function amplitude for ^{6}He+^{4}He elastic scattering at $E_{\rm lab}=151$ MeV. A plane wave of unit amplitude comes from the left (negative z values). An optical potential of the volume Woods-Saxon form was used with the parameter set 2 of Table I. The sum over 70 partial waves was done.

C. Distorted waves

The three-dimensional distorted waves entering the transition amplitude (3) were calculated within standard OM code by summing the radial partial waves with the Legendre polynomials [6]. The corresponding OM parameters were found by fitting the elastic-scattering cross section to experimental data (see below). The amplitude of the wave function describing elastic scattering of ^{6}He from ^{4}He at the laboratory energy of 151 MeV is shown in Fig. 2. A plane wave of unit amplitude comes in from the left side (negative z values in Fig. 2), the OM potential is located at the zero point. The imaginary part of the OM potential is responsible for the absorption of the wave in the elastic channel at small distances (when the projectile penetrates into the target) and for shadowing in the region behind the target nucleus. In collisions of not very heavy nuclei, when the de Broglie wavelength of their relative motion is not so small and the nuclei do not behave like black (absolutely absorbing) spheres, the trajectories deflected to negative angles make an appreciable contribution to the elastic-scattering cross section, and their focusing on the beam axis just behind the target nucleus leads to a sharp increase of the wave function amplitude, Fig. 2. This effect should also be taken into account when we calculate the transition amplitude (3).

Of course, an imaginary part of the OM potential (taken local and l independent) simulates the withdrawal of incoming flux from the elastic channel (absorption) only in some approximate way (reproducing decrease of the outgoing flux in the elastic channel at infinity) and cannot describe correctly a realistic channel coupling. It means that even a rather good fitting to the elastic-scattering cross section with a given set of OM parameters cannot assure unambiguously a correct behavior of the distorted wave at small distances, in particular, those focusing effects given by the trajectories in which the colliding nuclei pass through each other. Therefore, we should be careful with the contribution to the transfer cross section coming from the shadow regions of the distorted waves $\chi^{(\pm)}_{\mathbf{k}}(\mathbf{R})$.

Real and imaginary parts of the distorted waves oscillate rapidly in accordance with the value of the de Broglie wavelength $\lambda=2\pi/k_{i,f}$ of the ion-ion relative motion. Hence, we have to use sufficiently small integration steps—$\Delta R\ll\lambda$,

$R\Delta\theta \ll \lambda$, and $R\sin(\theta)\Delta\varphi \ll \lambda$—when calculating directly the nine-dimensional transition amplitude integral. The real resulting oscillations of the integrand (3) are determined by the difference $\mathbf{k}_i \cdot \mathbf{R}_i - \mathbf{k}_f \cdot \mathbf{R}_f$ [more exactly, by the difference of the classical action functions $S_i(\mathbf{k}_i \cdot \mathbf{R}_i) - S_f(\mathbf{k}_f \cdot \mathbf{R}_f)$ [7]] and, in fact, are much smaller at forward scattering angles [small values of the effective transferred momentum $\mathbf{q}_{\mathrm{eff}} = \mathbf{k}_i - (A_1/(A_1+2))\,\mathbf{k}_f$]. But at backward angles (large q_{eff} values) the oscillations can be even larger than the oscillations of the distorted waves themselves. These oscillations (radial and angular) create difficulties in the calculation of the transition amplitude, but the resulting angular distribution turns out to be more transparent compared with the method of partial wave decomposition, due to a possibility to see and compare directly the contributions coming to the cross section from the different regions of three-dimensional space, i.e., from the different spatial configurations of the four-body system (see below).

D. Three-body bound-state wave functions

A deep understanding of the exotic genuine few-body structure of halo nuclei is still of prime interest. The structure of nuclei far from the stability line (particularly those close to the neutron drip line) is a main subject of investigations in radioactive ion beam (RIB) experiments. For that purpose we use accurately calculated three-body bound-state wave functions $\Psi_i^{(234)}(\mathbf{x},\mathbf{y})$ from [1,8,9] for such nuclei as ^{6}Li, ^{6}He, ^{11}Li. In this approach the bound-state wave function is calculated within a three-body model (core$+N+N$) using an expansion over hyperspherical harmonics. It can be written in the following form:

$$
\begin{aligned}
\Psi^{JM}(\mathbf{x},\mathbf{y}) &= \rho^{-5/2} \sum_{\gamma} \chi_\gamma(\rho)\, \psi_K^{l_x l_y}(\alpha) \\
&\quad \cdot [[\mathbf{Y}_{l_x}(\hat{\mathbf{x}}) \otimes \mathbf{Y}_{l_y}(\hat{\mathbf{y}})]_L \otimes \mathbf{X}_S]_{JM} \\
&= \sum_{\gamma} \sum_{m_x M_S} (L M_L S M_S | JM) \\
&\quad \times (l_x m_x l_y m_y | L M_L) \cdot \rho^{-5/2} \chi_\gamma(\rho)\, \psi_K^{l_x l_y}(\alpha) \\
&\quad \cdot Y_{l_x m_x}(\hat{\mathbf{x}}) \cdot Y_{l_y m_y}(\hat{\mathbf{y}}) \cdot X_S(M_S),
\end{aligned} \tag{7}
$$

where $(j_1 m_1 j_2 m_2 | j_3 m_3)$ are Clebsh-Gordon coefficients, $M_L = M - M_S$, $m_y = M - M_S - m_x$, $X_S(M_S)$ is the coupled two-nucleon spin function ($S=0,1$). The channel indices are $\gamma \equiv l_x, l_y, L, S, K$, where $K = l_x + l_y + 2n$ ($n = 0,1,2,\ldots$) is the hypermoment. Polar angle-type variables are used where $\rho = \sqrt{\mu_{34} x^2 + \mu_{2(34)} y^2}$ is the hyperradius, $\alpha = \mathrm{arctg}(\sqrt{\mu_{34}}x/\sqrt{\mu_{2(34)}}y)$ is the hyperangle, $\mu_{34} = 1/2$ and $\mu_{2(34)} = 2 \cdot A_2/(A_2+2)$ ($=4/3$ in the case of ^{6}He or ^{6}Li) are the reduced masses intrinsic of the two-nucleon pair and of two nucleons with respect to the core. The hyperangular functions are

$$
\psi_K^{l_x l_y}(\alpha) = C_K^{l_x l_y} \cdot (\sin\alpha)^{l_x} (\cos\alpha)^{l_y} P_n^{l_x+1/2,\, l_y+1/2}(\cos 2\alpha), \tag{8}
$$

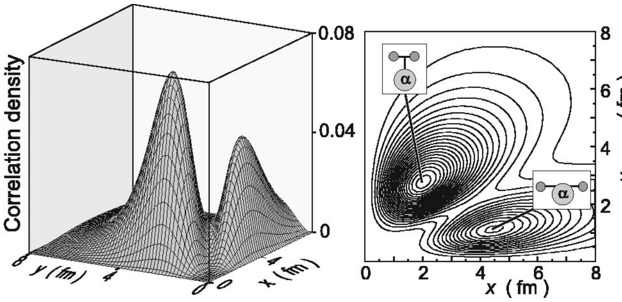

FIG. 3. Spatial correlation density plot for the ground state of ^{6}He. x is the distance between two valence neutrons and y is the distance from the α core to the (nn) center of mass. Dineutron and cigarlike components are clearly present.

where $P_n^{\tau\tau'}$ is the Jakobi polynomial, $C_K^{ll'}$ a normalizing coefficient. The radial functions $\chi_\gamma(\rho)$ are obtained from numerical solution of the three-body bound-state problem reduced to a set of coupled differential Schrödinger equations. The details of these calculations can be found in [1,8].

The binding energies of the nuclei can be reproduced rather well in such calculations with realistic two-body interactions found from the phase analysis of the corresponding elastic scattering plus some renormalization [9]. The resulting wave function which has appropriate asymptotic behavior in all regions of six-dimensional space, takes into account the Pauli principle between the valence nucleons and the nucleons of the core, and predicts accurately the nuclear radii. For the Borromean ^{6}He and ^{11}Li nuclei the halo structure of their ground states were found to have a very extended valence neutron density, much more extended than can be obtained in a shell-model picture.

In Fig. 3 the so-called spatial correlation density plot for the ground state of ^{6}He is shown (three-dimensional and topographical landscapes) in the $\mathbf{x}$ and $\mathbf{y}$ variables, where x is the distance between two valence neutrons and y is the distance from the α core to the (nn) center of mass

$$
P(x,y) = x^2 \cdot y^2 \cdot \int |\Psi_i^{(234)}(\mathbf{x},\mathbf{y})|^2 d\Omega_{\mathbf{x}} d\Omega_{\mathbf{y}}. \tag{9}
$$

The correlation plot exhibits two prominent peaks: a ‘‘dineutron’’like peak with the two valence neutrons located together outside the α particle ($x<y$), and a ‘‘cigarlike’’ peak with the valence neutrons positioned on opposite sides of the α particle ($x>y$). The corresponding configurations are shown schematically in the inset of Fig. 3. The origin of these spatial configurations is connected with dominance of $L=S=0$ motion in the 0^+ g.s. of ^{6}He and with the Pauli principle blocking the s motion (occupied in the α core and making the valence nucleons fill the $1p$ state in a shell-model picture). The difference in heights of the two components (Fig. 3) is mainly due to the n-n interaction making the dineutron configuration more probable. A ‘‘direct’’ experimental observation of this spatial two-component structure of ^{6}He which could determine relative weights of the dineutron and ‘‘cigarlike’’ components is of great interest. Good understanding of the structure of the ^{6}He nucleus may help us to understand better also the structures of other loosely bound nuclei, including ^{8}He and ^{10}He.

E. Expansion over harmonic oscillator states

The variables in the integrand of Eq. (3) can be partially separated by decomposition of the initial and final bound states $\Psi_{i,f}(\mathbf{x},\mathbf{y}_{i,f})$ over some complete set of functions depending on their common variable $\mathbf{x}$—the relative distance between the two transferred nucleons. For this purpose we use a complete set of two nucleon relative motion wave functions

$$\{F_{\nu=Nl_xm_xSM_S}(\mathbf{x})\}=\{f_{Nl_x}(x)\cdot Y_{l_xm_x}(\hat{\mathbf{x}})\cdot X_S(M_S)\},\qquad (10)$$

where $f_{Nl_x}(x)$ are the radial three-dimensional harmonic oscillator eigenfunctions.

Projecting the three-body wave function (7) on these two-nucleon states we obtain

$$\Psi^{JM}(\mathbf{x},\mathbf{y})=\sum_{\nu} F_\nu(\mathbf{x})\Phi_\nu^{JM}(\mathbf{y}),\qquad (11)$$

where

$$\Phi_\nu^{JM}(\mathbf{y})=\sum_{Ll_y}(LM_LSM_S|JM)\times(l_xm_xl_ym_y|LM_L)\cdot\phi_{Nl_xS(Ll_y)}(y)\cdot Y_{l_ym_y}(\hat{\mathbf{y}}),\qquad (12)$$

and where

$$\phi_{Nl_xS(Ll_y)}(y)=\sum_{K=l_x+l_y+2n}\int_0^\infty f_{Nl_x}(x)\cdot[\rho^{-5/2}\chi_\gamma(\rho)\psi_K^{l_xl_y}(\alpha)]x^2dx\qquad (13)$$

are the radial overlap integrals which have to be calculated numerically. The functions $\phi_{Nl_xS(Ll_y)}(y)$ describe the relative motion of the center of mass of the two nucleons in the field of the core.

The oscillator wave functions depend on only one parameter, the range $r_0=\sqrt{(3/2)(\hbar/\mu\omega)}$. In principle, any set of oscillator eigenfunctions $f_{Nl_x}(x)$ can be used (due to formal completeness of a set), but in practice we chose the oscillator range, i.e., $\hbar\omega$, in such a way that the rms two-nucleon separation in the ground state ($Nl_x=00$) is close to the value extracted for the the projectile from a realistic three-body calculation (for ^{6}He, for example, $\overline{x}_{nn}\sim 4.5$ fm [1]). In this case the series over ν in Eq. (11) converges very fast and only a few components need to be kept in the sum to describe sufficiently well the main properties of the bound-state wave function. The norm of the function $\Phi_\nu(\mathbf{y})$ serves as a criterion for the truncation in Eq. (11), and the residual terms have to provide the total normalization of $\Psi^{JM}(\mathbf{x},\mathbf{y})$ close to unity.

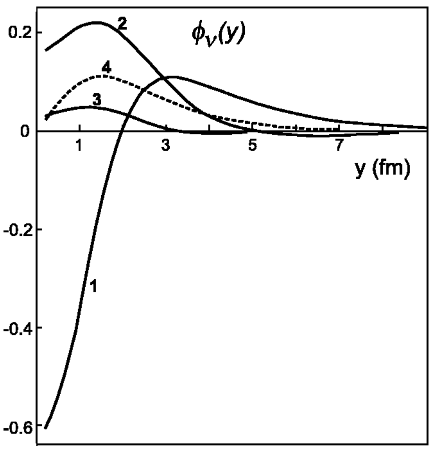

FIG. 4. Decomposition of the ^{6}He bound-state wave function corresponding to the relative motion of the two-neutron pair and α core—see Eq. (13) of the text. The curves 1–4 correspond to states with quantum numbers $N,l_x,S=(000)$, (200), (400), and (111).

For some nuclei the expansions (11) and (12) turn out to be very simple. In particular, the ground state of ^{6}He has $J^\pi=0^+$ and the total orbital momentum L has only two values $L=0(S=0)$ and $L=1(S=1)$. Moreover, due to strict antisymmetry between the two valence nucleons the orbital momenta l_x and l_y (corresponding to the relative n-n motion and to the motion of their center of mass with respect to the α core) have to be equal ($l_x=l_y$) and to have a parity equal to the parity of total L [1]. Thus, in fact, there is no summing over L,l_y in Eq. (12). It was shown that the component $SLl_x=(000)$ brings about 84% to the total normalization of $\Psi^{JM}(\mathbf{x},\mathbf{y})$ and the component $SLl_x=(111)$—about 13.5% [1]. We found that four components of the decomposition (11)—those with $Nl_xS=(000),(200),(400)$, and (111)—are enough to give 92% to the total normalization of ^{6}He, ground-state wave function. These components are shown in Fig. 4. The component $\phi_{Nl_xS(Ll_y)=000(00)}$ dominates and looks like the pure $2s$ state of (nn)-α relative motion used in the first simplified estimation of the two-neutron transfer reaction [4]. Note, that all the functions $\phi_\nu(y)$ have an appropriate asymptotic behavior $\sim\exp(-\kappa y)/y$ at $y\gg x$, where $\kappa=\sqrt{2\mu_{2(34)}E_{\rm sep}/\hbar^2}$ and $E_{\rm sep}$ is the two-nucleon separation energy.

Substituting expansion (11) into Eq. (3) we write the transition amplitude in the form

$$T_{fi}^{\rm DWBA}(\mathbf{k}_f,\mathbf{k}_i)=\sum_{\nu',\nu}\langle\chi_{\mathbf{k}_f}^{(-)}(\mathbf{R}_f)\cdot\Phi_{\nu'}^{J_fM_f}(\mathbf{y}_f)\times|\Delta V_{\nu',\nu}(\mathbf{y}_f,\mathbf{y}_i)|\times\Phi_\nu^{J_iM_i}(\mathbf{y}_i)\cdot\chi_{\mathbf{k}_i}^{(+)}(\mathbf{R}_i)\rangle,\qquad (14)$$

where

$$\Delta V_{\nu',\nu}(\mathbf{y}_f,\mathbf{y}_i)=\int f_{N'l'_x}(x)Y^*_{l'_xm'_x}(\hat{\mathbf{x}})X^\dagger_{S'}(M'_S)\cdot\Delta V\cdot f_{Nl_x}(x)\times Y_{l_xm_x}(\hat{\mathbf{x}})X_S(M_S)d^3\mathbf{x}\qquad (15)$$

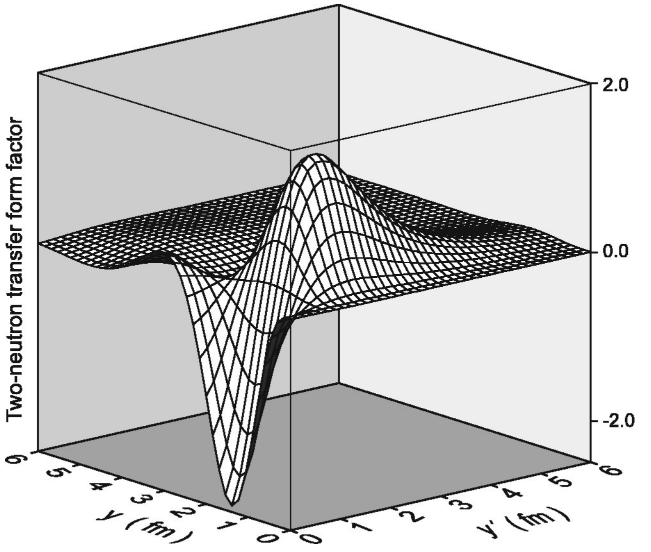

FIG. 5. The form-factor of the two-neutron transfer reaction ^{4}He(^{6}He,^{4}He)^{6}He: $\Sigma_{\nu',\nu}\Phi_{\nu'}(y')\Delta V_{\nu'\nu}(y)\Phi_\nu(y)\cdot y^2, \nu',\nu$ $(=Nl_xS)=(000)$, (200), and (400).

and where the interaction ΔV is chosen in the post Eq. (4) or prior Eq. (5) representation. Neglecting spin-orbital interaction in ΔV we have $\Delta V_{\nu',\nu} \sim \delta_{SS'}\delta_{M_S M_S'}$. If the spins J_i, J_f are not equal to zero, summation over M_f and averaging over M_i have to be done in the cross section (6).

F. Reaction form-factor

As can be seen from Eq. (14) the process of two-nucleon transfer is determined by the distorted waves in the entrance and exit channels $\chi^{(\pm)}_{\mathbf{k}_{i,f}}(\mathbf{R}_{i,f})$ and by the nonlocal form factor of the reaction,

$$F(\mathbf{y}_f,\mathbf{y}_i)=\sum_{\nu',\nu}\Phi^{J_fM_f}_{\nu'}(\mathbf{y}_f)\Delta V_{\nu',\nu}(\mathbf{y}_f,\mathbf{y}_i)\Phi^{J_iM_i}_{\nu}(\mathbf{y}_i). \tag{16}$$

In heavy-ion collisions, when the masses of the heavy cores are much greater then the transferred mass $(A_1,A_2 \gg 2)$, the so-called no-recoil approximation can be used (see, for example, [10]). In this case $\mathbf{R}_i \approx \mathbf{R}_{12}$, $\mathbf{R}_f \approx [A_1/(A_1+2)]\mathbf{R}_{12}$, and the integration over $\mathbf{y}_i$ in Eqs. (14) and (16) can be performed independently of $\mathbf{R}_i$. Now the reaction form factor depends only on one variable $\mathbf{R}_{12}=\mathbf{y}_f-\mathbf{y}_i$, and the transition amplitude (14) is reduced to an easily calculated three-dimensional integral. We intend to apply our approach for a description of two-nucleon transfer processes with light ions, such reactions as ^{6}He+^{4}He, ^{6}He+^{1}H, ^{8}He+^{4}He, and so on. Therefore, we cannot use the no-recoil approximation in any form and have to calculate the six-dimensional integral (14) with the nonlocal form factor (16) directly without further simplifications.

The behavior of the form factor (16) in two-dimensional space can be understood better from Fig. 5, where it is shown for the two-neutron transfer reaction ^{4}He(^{6}He,^{4}He)^{6}He. For simplicity, only the main component of the ^{6}He ground state with $L,S=0,0$ was taken into account and only the "stripping" part of the post-representation interaction $V_{23}(\mathbf{y}_i+\mathbf{x}/2)+V_{24}(\mathbf{y}_i-\mathbf{x}/22)$ was used in Eq. (15) to calculate the form factor (16). In this case we can restrict the sum over ν',ν to $l_x=l_x'=0$, and $F(\mathbf{y}_f,\mathbf{y}_i)$ does not depend on the orientations of the vectors $\mathbf{y}_f,\mathbf{y}_i$, but only on their lengths. Taking into account the three-dimensional integration over $\mathbf{y}_i$ in Eq. (14) we multiplied the form factor shown in Fig. 5 by y_i^2. Figure 5 shows that the two-neutron transfer form factor decreases very fast with increasing y_i (in spite of multiplication by y_i^2) due to the short-range potentials of the neutron-α interactions V_{23} and V_{24}, and it decreases slowly with increasing y_f due to the weak slope of the wave function describing two-neutron separation from the α core—$\phi_\nu(y_f) \sim \exp(-\sqrt{2\mu_{1(34)}E_{\text{sep}}/\hbar^2}y_f)/y_f$, with $E_{\text{sep}}=0.973$ MeV.

This means that in the post representation of the transition amplitude the argument y_i of the two-dimensional two-neutron transfer form factor (16) reflects mainly the properties of the interaction responsible for the transfer process, while the argument y_f reflects the properties of the final two-nucleon bound state in the residual nucleus: $\Phi^{J_fM_f}_{\nu'}(\mathbf{y}_f)$. In particular, the dominant $2s$ structure of the two-neutron center-of-mass motion in the ^{6}He ground state can be seen in Fig. 5 along the variable $y' \equiv y_f$. Thus, if we want to study in detail the structure of a nucleus formed in the transfer reaction (ejectile), we should use the post representation of the DWBA transition amplitude, integrating over $\mathbf{y}_i$ and $\mathbf{R}_i$ in Eq. (14). But, if we are interested first of all in the structure of the projectile or target (for example, in the ^{6}He+^{1}H reactions), the prior form of the transition amplitude is preferable with $\Delta V=V_{13}(\mathbf{y}_f+\mathbf{x}/2)+V_{14}(\mathbf{y}_f-\mathbf{x}/2)$ in Eq. (15) and with an integration over $\mathbf{y}_f$ and $\mathbf{R}_f$ in Eq. (14). Below we apply our four-body approach to a description of the two-neutron transfer process in the ^{4}He(^{6}He ^{4}He)^{6}He and ^{1}H(^{6}He ^{4}He)^{3}H reactions. In the first case the post and prior forms of the transition amplitude are naturally identical, and in the second one, with formation of a triton in the exit channel, we choose the prior representation paying attention just to the three-body function of ^{6}He. Of course, accurate calculations of the DWBA transition amplitude (3) both within post Eq. (4) and prior Eq. (5) representation should bring us the same results if the wave functions $\Psi^{(234)}_i(\mathbf{x},\mathbf{y}_i)\cdot\chi^{(+)}_{\mathbf{k}_i}(\mathbf{R}_i)$ and $\Psi^{(134)}_f(\mathbf{x},\mathbf{y}_f)\cdot\chi^{(-)}_{\mathbf{k}_f}(\mathbf{R}_f)$ are the exact eigen-functions of the Hamiltonians $H_i=H_0+V_{23}+V_{24}+U^{\text{OM}}_i$ and $H_f=H_0+V_{13}+V_{14}+U^{\text{OM}}_f$ correspondingly. However, since we use model three-body bound-state wave functions $\Psi^{(234)}_i$ and $\Psi^{(134)}_f$ (see below), the post and prior transition amplitudes can differ somewhat from each other (see, e.g., [11]). This problem as well as other methodical questions specific for the four-body three-dimentional DWBA approach will be discussed in our forthcoming paper.

G. ^{4}He+^{6}Li elastic scattering

The ^{6}Li nucleus has a three-body structure similar to that of ^{6}He [1]. The "deuteron halo" is somewhat less impressive because of the difference between n-n and n-p interactions, but the deuteron separation energy from ^{6}Li is small

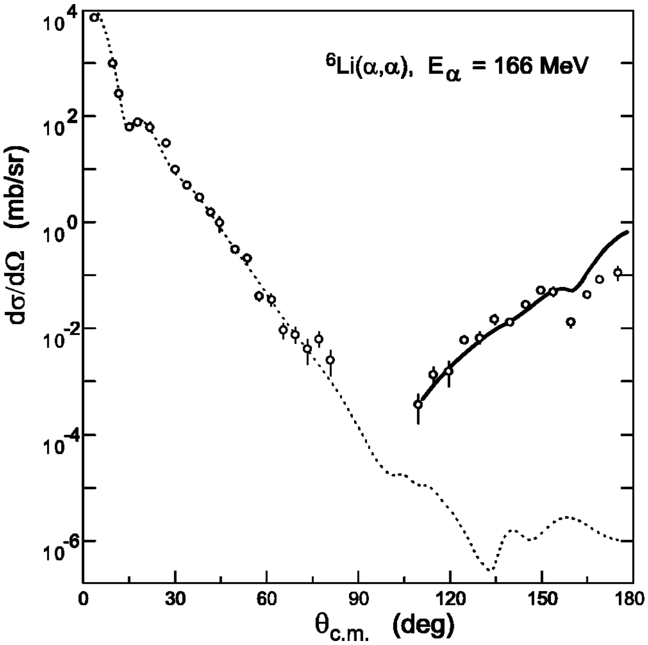

FIG. 6. Elastic scattering $\alpha+{}^6\mathrm{Li}$ at $E_\alpha^{\mathrm{lab}}=166\,\mathrm{MeV}$. The dotted curve shows the optical-model fit with the parameters from Table I. The solid curve corresponds to the four-body DWBA calculation of ''ground state–ground state'' deuteron transfer.

also in comparison with neutron and proton separation energies, $E_d^{\mathrm{sep}}({}^6\mathrm{Li})\approx 1.5$ MeV, $E_n^{\mathrm{sep}}({}^6\mathrm{Li})\approx 5.7$ MeV, and $E_p^{\mathrm{sep}}({}^6\mathrm{Li})\approx 4.6$ MeV, and the deuteron is loosely bound also within ^{6}Li. It means that ^{6}Li resembles features of ^{6}He, moreover, its excited state 0^+(3.56 MeV) belongs to the same isobaric triplet as ^{6}He (g.s.) and ^{6}Be(g.s). So, we will use the well-studied reactions induced by ^{6}Li as a starting point for comparison of similar reactions induced by ^{6}He. In [12] the elastic scattering of 166 MeV ^{4}He from ^{6}Li was measured in the full center-of-mass angular region, reproduced in Fig. 6. The backward angle elastic scattering cannot be described within the standard optical model and was understood as the exchange of a deuteron cluster between two α cores.

With the same optical-model parameters [12] (set 1 of Table I) we repeated the $^4\mathrm{He}+{}^6\mathrm{Li}$ elastic-scattering calculation and got the rather good fit of the forward angle elastic-scattering experimental data shown in Fig. 6. By no reasonable changes of these parameters can the backward angle yield of α particles be simultaneously described. The difference between the calculated OM cross section of the potential elastic scattering and the backward experimental data is about four orders of magnitude. This leads us to infer that in this reaction the backward angle α particles are formed preferably in a ground-ground deuteron exchange process (1), where 1 and 2 are α particles and (3,4) a deuteron. Using the ^{6}Li ground-state wave function obtained in [1] and Gaussian shape neutron-α and proton-α interactions with $V_0^{N\alpha}=-47\,\mathrm{MeV}$, $b=2.3\,\mathrm{fm}$ (plus the Coulomb interaction in the case of $V_{p\alpha}$), we calculated the cross section of the two-nucleon transfer process within our four-body approach (full finite range (FR)+all recoil effects), the solid curve in Fig. 6. We should sum up coherently the amplitude of the potential elastic scattering and the two-nucleon transition amplitude with the formation of the residual nucleus in its ground state to obtain the real elastic-scattering cross section in the whole angular region

$$\frac{d\sigma_{fi}}{d\Omega}(\theta)\sim\left|T^{\mathrm{OM}}(\theta)+\sqrt{S_f S_i}\cdot T_{fi}(\pi-\theta)\right|^2. \tag{17}$$

However, at beam energies higher than 20 MeV/nucleon the backward elastic potential scattering cross section is found to be several orders of magnitude smaller than the transfer cross section, see Fig. 6, and we can easily distinguish them. In the angular region of 80°–100° there should be interference (not calculated here) of the two different processes. At low beam energies (less than 10 MeV/nucleon) such interference will be important in a wide angular region. The analysis of the reaction will then be more complicated, and it will be difficult to distinguish between the two processes. As can be seen from Fig. 6, the proposed three-dimensional four-body approach to the direct two-nucleon transfer reactions enables us to obtain a rather good description of the transfer of a deuteron from the ^{6}Li nucleus to the α-particle target with formation of the ground-state ^{6}Li ejectile. So, we will apply the same approach to the analysis of similar reactions induced by the loosely bound Borromean nuclei like ^{6}He, ^{8}He, or ^{11}Li.

III. ^{6}He+^{4}He COLLISION

In the Flerov Laboratory of Nuclear Reactions a secondary beam of ^{6}He with energy of 151 MeV was produced by fragmentation of 32 MeV/nucleon ^{7}Li ions on a thick ^{9}Be target. The quality of the ^{6}He beam was rather good and its intensity amounted to about 10^5 particles/s. The ions of ^{6}He were separated with the ACCULINNA facility [13] commissioned at the U-400M cyclotron. This experimental setup consists of two silicon detector telescopes and allows one to measure in coincidence two reaction products with a good energy and angular resolution, about 100 keV and $\pm 2°$, respectively. The first experiments with the ^{6}He beam were done on ^{4}He [4] and ^{1}H targets [5], and quite interesting results have been obtained.

TABLE I. Optical-model parameters for $^6\mathrm{Li}+{}^4\mathrm{He}$ and $^6\mathrm{He}+{}^4\mathrm{He}$ elastic scattering.

Set	E_{lab}(MeV)	V_0^{vol}(MeV)	R_V(fm)	a_V(fm)	W_0^{vol}(MeV)	R_W(fm)	a_W(fm)
1,^{4}He+^{6}Li	166	−102.5	1.78	0.820	−11.8	4.11	0.950
2,^{6}He+^{4}He	151	−102.5	1.78	0.920	−13.0	3.85	0.500
3,^{6}He+^{4}He	151	−102.5	1.54	0.904	−7.0	4.28	0.569

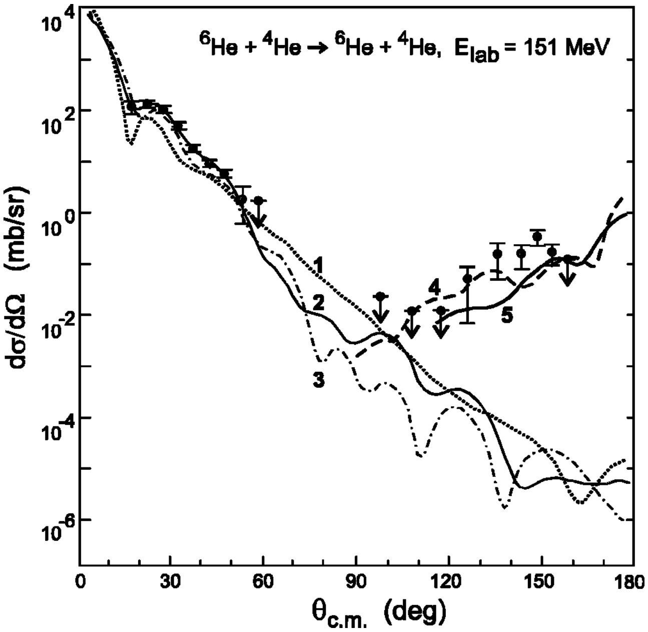

FIG. 7. The ^{6}He+^{4}He elastic scattering at $E_{\rm lab}$=151 MeV. The dotted curve 1 shows the optical-model calculation with the same parameters as for ^{6}Li+^{4}He (see Table I), the solid curve 2 corresponds to the OM fit with the parameters of set 2, and the dot-dashed curve 3 was obtained with the real double-folding potential of the ^{6}He+^{4}He interaction proposed by Baye *et al.* [14] and with the imaginary part of set 2 (Table I). The dashed curve 4 shows the result of the simplified calculation of the $2n$-cluster exchange [Eq. (18)], and curve 5 is obtained within the four-body model of the two-neutron transfer reaction [Eq. (14)].

A. Elastic scattering and two-neutron exchange

The elastic scattering ^{6}He+^{4}He at beam energy of 151 MeV was measured at forward and backward center-of-mass angles [4]. Note, that the backward angle elastic scattering cross section was extracted from the coincident events when both the ejectiles (^{6}He and ^{4}He) were detected. A possible contribution of inelastic scattering is prevented by the fact that all the excited states in the collision partners, ^{6}He and ^{4}He, are unstable with respect to particle emission. For the backward angles the total number of accumulated coincident events allowed extraction of a differential cross section larger than about 0.01 mb/sr. The final experimental results are shown in Fig. 7.

To analyze these results, we again first described the forward angle data within the optical model. Unfortunately, the available forward angle elastic-scattering cross sections were only measured in a rather narrow c.m. angular region of 17°–59°. Thus, we cannot carry out a fitting of these data which gives reliable OM potential parameters. Instead, we took as a starting point the OM potential that was found for ^{4}He+^{6}Li elastic scattering at $E_{\rm lab}$= 166 MeV [12], see Table I. The differential cross section calculated for the ^{6}He+^{4}He system with these OM parameters is shown in Fig. 7 by the dotted line (curve 1). The calculated curve falls below the forward angle experimental points by about 30%. By a small adjustment of the OM potential parameters we were able to eliminate this discrepancy as shown by the solid curve (2) in Fig. 7 which corresponds to the OM calculation with the new potential parameters listed in Table I, set 2. The variations of the OM parameters are, in view of the difference between ^{6}He and ^{6}Li, quite reasonable. Experimental data on the elastic-scattering cross section in a wider forward angle region are required to obtain more reliable OM potential parameters of the ^{6}He+^{4}He interaction. Finally, we calculated the elastic-scattering cross section with the real double-folding potential proposed by Baye *et al.* [14] for the ^{6}He+ ^{4}He interaction. Note, that the depth of this double-folding potential (−99.72 MeV) is very close to the phenomenological one (−102.5 MeV). An imaginary part of OMP was not proposed in [14] and we used the parameters of set 2 of Table I. The result of this calculation is shown in Fig. 7 by the dot-dashed curve 3.

In the backward angular range of $\theta_{\rm c.m.} \geqslant 130°$ the potential elastic-scattering cross section calculated within standard OM code is less than 10^{-4} mb/sr and decreases with increasing angle, whereas experimental values are higher than 10^{-1} mb/sr, i.e., about three orders of magnitude more. As was expected, there is no reasonable set of OM parameters that could reproduce the backward yield of the ^{6}He nuclei observed at so high incident energy. A change in the calculated values of the differential cross section by a factor of 3–10 for some local angular intervals in the backward hemisphere is the maximum that one can achieve by varying the OM parameters. This definitely means that the ^{6}He elastic-scattering events observed in this backward angular region are in fact the result of two-neutron exchange with the ^{4}He target nucleus.

Using the OM parameters of Table I (set 2) and the spin-independent neutron-α interaction ($V_{23}=V_{24}=V_{\alpha n}$) of Gaussian shape with depth of -47.32 MeV and width b $=2.4$ fm, we calculated the cross section of the two-neutron transfer process in the reaction ^{6}He+^{4}He→^{4}He+^{6}He (g.s.) within our more consistent four-body three-dimensional approach. Because the nuclei formed in this reaction are the same ones as in the entrance channel and they are in the ground states, the transfer reaction, in fact, manifests itself as an elastic scattering to the center-of-mass angle $\theta=\pi-\theta_{\rm exch}$. As in the case of ^{4}He+^{6}Li (Sec. II G), we did not sum coherently the amplitude of the elastic scattering and the transition amplitude of two-neutron exchange [see Eq. (17)] because their values differ drastically at backward angles—$|T^{\rm OM}(\theta\sim\pi)|\ll|T_{fi}^{\rm DWBA}(\theta\sim 0°)|$. At the angles of 80°–100° such interference would be very important and has to be taken into account if details of the angular distribution in this region are to be reproduced. The two-neutron exchange cross section calculated with Eqs. (6) and (14) is shown in Fig. 7 by the solid curve 5.

The first estimation of the two-neutron transfer cross section was done in [4] within a simplified approach in which the two neutrons in ^{6}He were treated as a cluster described by a wave function depending on the $\mathbf{y}_{nn-\alpha}$ coordinate only. The transition amplitude was taken in the form

$$T_{fi}^{\rm DWBA}(\mathbf{k}_f,\mathbf{k}_i)=\langle\chi^{(-)}_{\mathbf{k}_f}(\mathbf{R}_f)\Phi^{\rm mod}_{2n}(\mathbf{y}_f)|V_{(2n)\alpha}(\mathbf{y}_i)| \times\Phi^{\rm mod}_{2n}(\mathbf{y}_i)\chi^{(+)}_{\mathbf{k}_i}(\mathbf{R}_i)\rangle \qquad (18)$$

and the normalized model $2n$-cluster wave function $\Phi_{2n}^{\mathrm{mod}}(\mathbf{y})$ was calculated within a Woods-Saxon potential $V_{(2n)\alpha}$ with radius of 2 fm and diffuseness of 0.5 fm. The depth of this potential was adjusted to reproduce a $2s$ state with a two-neutron separation energy of 0.973 MeV.

Comparison of the calculated values of the reaction cross section (made within the simplified $2n$-cluster model and within the four-body approach) with the experimental data allows us to conclude that (i) the $2n-\alpha$ configuration of the ^{6}He nucleus with a weight close to unity, i.e., the spectroscopic factor $S_{(2n)\alpha}(^6\mathrm{He})\approx 1$ is compatible with the data, and (ii) the structure of this three-body configuration is sufficiently well described by the wave function proposed in [1,8,9], see Eq. (7) and Fig. 3. Comparison of the ''three-body'' transition amplitude (18) with the ''four-body'' one (14) shows that the model $2n$-cluster wave function $\Phi_{2n}^{\mathrm{mod}}(\mathbf{y})$ corresponds roughly to the $\nu(=N,l,S)=(000)$ component (normalized to unity) of the expansion (11). Because this is the main component of the real three-body wave function of the ^{6}He bound state—see curve 1 in Fig. 4—the $2n$-cluster transfer cross section calculated with Eq. (18) does not deviate drastically from the full calculation, see dashed line 4 in Fig. 7. Both are compatible with the experimental data. Data of higher quality are needed for a more detailed assessment of the success of our reaction model in this case.

B. Dynamics of $2n$ transfer reaction

By slightly varying the OM potential parameters and (or) the parameters of the interactions ΔV we could improve our fit to the backward-angle experimental data in the two-neutron transfer (see below), but the rather large experimental errors and the reaction cross sections limited to the angular interval of 125°–158° does not justify this effort. Instead we try here to dissect the mechanism and the dynamics of the reaction. For simplicity, hereafter we analyze the two-neutron transfer cross section itself, i.e., the center-of-mass angular distribution of the ejectiles (here ^{4}He) formed in the reaction from the projectile nuclei ^{6}He, as one usually does. At the energies under consideration, such a reaction angular distribution has a common forward direction.

1. Dineutron versus cigarlike component

First of all we tried to explore the sensitivity of the two-neutron transfer cross section to the double-peak spatial structure of ^{6}He, Sec. II D. From a common consideration the ''dineutron'' component should dominate in the two-neutron transfer reactions, whereas the ''cigarlike'' configuration can be preferable in reactions with only one neutron being initially stripped from ^{6}He. These two possible configurations are present simultaneously in the bound-state wave function of ^{6}He (7) and cannot be clearly separated. They reflect simply the monopole nature of $1p$ states occupied by the two valence neutrons of ^{6}He. This is especially clear within the cluster-orbital shell-model approximation (COSMA) [1,15,16]. Switching off the neutron-neutron interaction and introducing one-particle oscillator functions for neutron-core relative motion $f_{nl}(r_k)\sim r_k\cdot\exp(-\beta r_k^2)(k=1,2)$ we can write the ^{6}He bound-state wave function in the following approximate form:

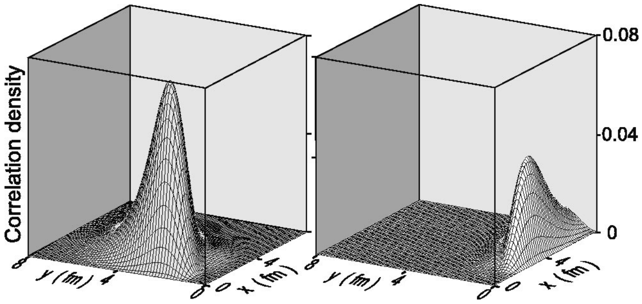

FIG. 8. Correlation density plots for the ground state of ^{6}He projected onto the dineutron (left) and cigarlike (right) configurations, see Eq. (20) of the text. x is the distance between two valence neutrons and y is the distance from the α core to the (nn) center of mass.

$$\begin{aligned}\Psi^{00}(\mathbf{r}_1,\mathbf{r}_2)&=\sum_m\ (1m1-m|00)\cdot f_{11}(r_1)\cdot f_{11}(r_2)\cdot Y_{1m}(\hat{\mathbf{r}}_1)\\&\quad\cdot Y_{1-m}(\hat{\mathbf{r}}_2)\cdot X_{S=0}\\&\sim(\mathbf{r}_1\cdot\mathbf{r}_2)e^{-\beta(r_1^2+r_2^2)}\\&\sim[y^2-(x/2)^2]e^{-2\beta[y^2+(x/2)^2]},\end{aligned}\tag{19}$$

where $\mathbf{y}=(\mathbf{r}_1+\mathbf{r}_2)/2$ is the position of the two-neutron center of mass relative to the α core and $\mathbf{x}=\mathbf{r}_1-\mathbf{r}_2$ is the distance between the neutrons, i.e., $\mathbf{y}$ and $\mathbf{x}$ are the same coordinates as in Eqs. (7) and (9) and in Fig. 3. So, as can be easily seen from Eq. (19), in the absence of the V_{nn} interaction the $L=S=0$ COSMA model function has a spatial correlation density with two distinguishable maxima of equal height and only the neutron-neutron interaction makes the dineutron component of the ^{6}He bound-state wave function more pronounced.

To find the contributions of these two peaks to the two-neutron transfer cross section we have to project in some way the total wave function (7) onto the dineutron and cigarlike configurations. As can be seen from Fig. 3 and Eq. (19) the two configurations are located on the different sides of the nodal line $y=\gamma x$ ($\gamma=1/2$). Introducing the coordinate $\xi=(\gamma x-y)/\sqrt{1+\gamma^2}$ which changes along the path orthogonal to the node line $y=\gamma x$, we may define operators $\hat{P}_{\mathrm{din}}=[1+\exp(\xi/\xi_0)]^{-1}$ and $\hat{P}_{\mathrm{cig}}(=1-\hat{P}_{\mathrm{din}})=[1+\exp(-\xi/\xi_0)]^{-1}$, which approximately divide the total three-body wave function (7) into dineutron and cigarlike parts

$$\Psi_{^6\mathrm{He}}(\mathbf{x},\mathbf{y})=\Psi_{^6\mathrm{He}}^{\mathrm{din}}+\Psi_{^6\mathrm{He}}^{\mathrm{cig}}\equiv\hat{P}_{\mathrm{din}}\Psi_{^6\mathrm{He}}+\hat{P}_{\mathrm{cig}}\Psi_{^6\mathrm{He}}.\tag{20}$$

To avoid the artificial oscillations that a sharp cutoff would introduce, we use the Fermi-type projection given above. Although the two components are not orthogonal to each other, their overlap is found to be less than 12% if we choose the x-independent parameter $\xi_0=0.65$ fm or less, see Fig. 8.

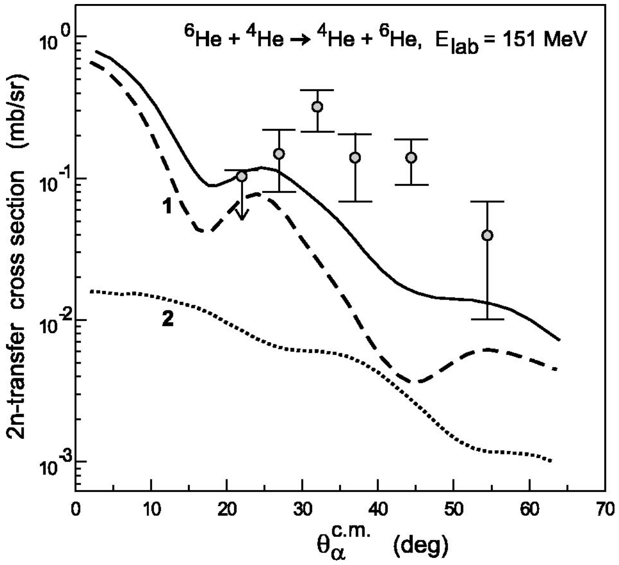

FIG. 9. The ^{4}He(^{6}He,^{4}He)^{6}He(g.s.) two-neutron transfer reaction at $E_{\rm lab}=151$ MeV. The dashed curve 1 is the contribution to the cross section coming from the dineutron configuration of ^{6}He and the dotted curve 2 is the contribution of the cigarlike component (see the text).

Inserting the wave functions $\Psi^{\rm din}_{^6{\rm He}}=\hat{P}_{\rm din}\Psi_{^6{\rm He}}$ and $\Psi^{\rm cig}_{^6{\rm He}}=\hat{P}_{\rm cig}\Psi_{^6{\rm He}}$ separately into the transition amplitude (3) instead of $\Psi_f^{(134)}(\mathbf{x},\mathbf{y}_f)$ and keeping the total wave function for $\Psi_i^{(234)}(\mathbf{x},\mathbf{y}_i)$ (to keep the normalization), we calculated the contributions of the dineutron and cigarlike configurations to the two-neutron transfer cross section of the ^{4}He(^{6}He, ^{4}He)^{6}He reaction. Figure 9 shows that the contributions of the two components are quite different. At all the forward angles the dineutron configuration of ^{6}He regulates the two-neutron transfer reaction. This reflects both the large weight of this configuration in the ground state of ^{6}He and a predominant surface localization of the two-neutron transfer process, leading to forward emission of the ejectiles. With increasing scattering angle (i.e., with increasing transferred momentum) the contribution of smaller impact parameters to the transfer cross section becomes larger and the role of the cigarlike configuration (located closer to the core) increases.

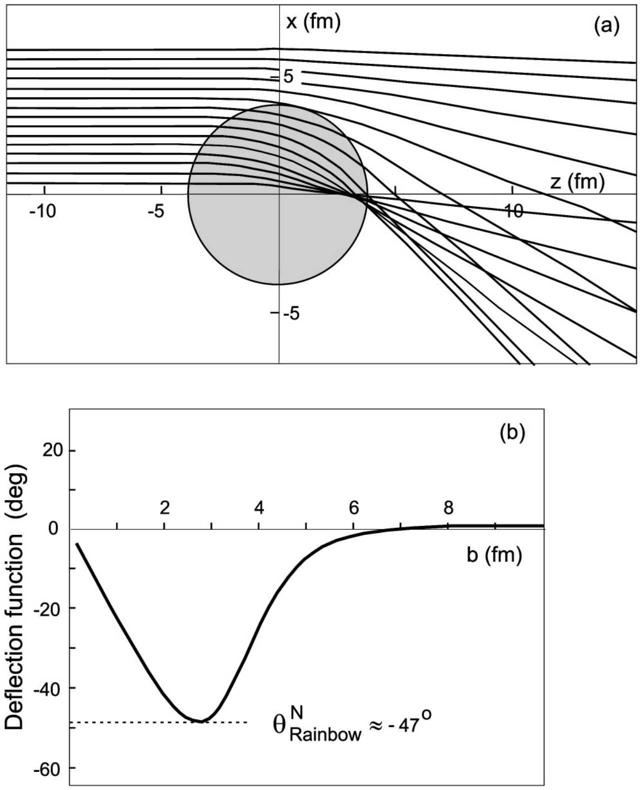

FIG. 10. Classical trajectories (a) and deflection function (b) of the ^{6}He+^{4}He elastic scattering at $E_{\rm lab}=151$ MeV. The shadowed circle shows the radius of the absorptive potential (see Table I).

2. Mean-field focusing and shadowing

Figure 2 shows that the distorted wave of ^{6}He elastically scattered from ^{4}He reflects both refractive and absorptive properties of the OM potential. The de Broglie wavelength of ^{6}He$-^4$He relative motion is about 1.2 fm at laboratory energy of 151 MeV. Therefore, classical features of the motion have to be noticeable, in particular, the field of the classical trajectories (shown in Fig. 10) should define the amplitude of the wave function [7]. For light nuclei like ^{6}He $+^4$He the attractive part of the interaction dominates at low energies, leading to deflection of the particles mainly to negative angles, see Fig. 10. It means that the grazing angle, so specific for heavy-ion collisions, is close to zero here and the grazing impact parameter is about 6 fm, i.e., greater than the sum of the radii of the colliding nuclei. The maximal negative deflection angle (the ''nuclear rainbow'' angle) is about $-47°$ and corresponds to impact parameter $b_R \approx 2.6$ fm at which the colliding nuclei strongly overlap and leave the elastic channel. Focusing of the trajectories on the beam axis in the region behind the target leads to the caustic-cusp surface and to a sharp increase of the amplitude of the distorted wave in this region.

Absorption (caused by channel coupling and simulated by the imaginary part of the OMP) reduces the contribution of those trajectories which go through the region of strong interaction. In the case of ^{6}He$+^4$He scattering such absorption is not so large, the shadow behind the absorptive sphere is not completely black, and the focusing effects of the attractive interaction remain visible, see Figs. 11 and 2. Because $\chi_{\mathbf{k}}^{(-)*}=\chi_{-\mathbf{k}}^{(+)}$, the shadow of the outgoing distorted wave is located in front of the absorptive sphere, and, as a result, there are four spatial regions giving the main contribution to the transition amplitude (14). Two of them (1 and 3 in Fig. 11) are due to comparatively weak absorption and focusing effects which are specific features of light ion scattering. Regions 2 and 4 are of common nature and correspond to the so-called ''near-far'' decomposition of the transition amplitude. Choosing the direction of the outgoing particle (moving along $\mathbf{k}_f$) as ''positive,'' we see that the outgoing wave originating from region 2 corresponds to negative deflection and those from region 4 correspond to positive deflection. Taking into account that the interaction potential of ^{6}He and ^{4}He is not able to deflect the nuclei into positive angles at the energy of 150 MeV (see Fig. 10), the contribution of

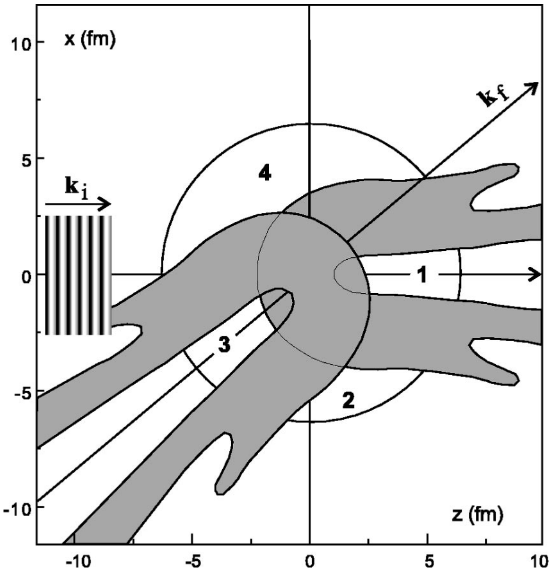

FIG. 11. Shadow regions of incoming (from the left) and outgoing distorted waves in the $^6He+^4He \rightarrow ^4He+^6He$ transfer reactions at $E_{\mathrm{lab}}=151$ MeV. In the shadowed regions the amplitudes of distorted waves $\chi^{(\pm)}_{\mathbf{k}_{i,f}}(\mathbf{R})$ are less than $\frac{1}{2}$. In regions 1 and 3 incoming and outgoing distorted waves are focused by the attractive interaction of ^6He with ^4He, see Fig. 2.

region 4 to the transfer cross section has to decrease with increasing exit angle and faster than the contribution coming from region 2 (see below).

Here we pay special attention to the contributions of regions 1 and 3 to the total transfer cross section. We do so because we do not know the real mechanism of absorption (to know it we have to solve the problem of channel coupling involving the Borromean continuum), and the imaginary part of OMP can only simulate in some approximate way a reduction of outgoing flux in the elastic channel at infinity. Moreover, we cannot confirm confidently that parameters of the absorptive potential (see Table I) have precisely their values, because available experimental data on elastic scattering of $^6He+^4He$ are insufficient for a conclusive parameter fitting. Thus, the real shadowing could be somewhat different from that shown in Fig. 11. In particular, if we eliminate the contributions of regions 1 and 3 (strong absorption, complete shadowing the focusing effect), then the total transfer cross section has a strong oscillation behavior at forward angles originating from interference of the waves coming from regions 2 and 4, see Fig. 12. The focusing effects and weak absorption leading to ''incomplete shadowing'' (regions 1 and 3) are rather important features of nuclear reactions with light ions.

3. Spatial localization of the reaction

Using our ''four-body three-dimensional'' approach without expansion of all the functions over partial waves (a procedure, which, as a rule, hides the dynamics of the process if many partial waves have to be taken into account), we can easily and directly analyze spatial localization of the two-neutron transfer reaction and also the dominant spatial configurations of the four-body system, thus focusing on the main contribution to the cross section at different angles. In particular, by restricting the integration over $\mathbf{R}_i$ in transition amplitude (14) to some part of the total space, we can estimate a probability for the process to occur just in this part of space. Of course, such restriction of integration has to be done quite accurately to avoid artificial oscillations of the result appearing in any sharp cutoff procedure. For this purpose, we used a smooth cutting function $f(\mathbf{R})$ equal to unity in a given part of the space and gradually going to zero at the boundary. This function should everywhere fulfill the condition $|\Delta f(\mathbf{R})|\cdot\lambda<1$, where λ is the de Broglie wavelength.

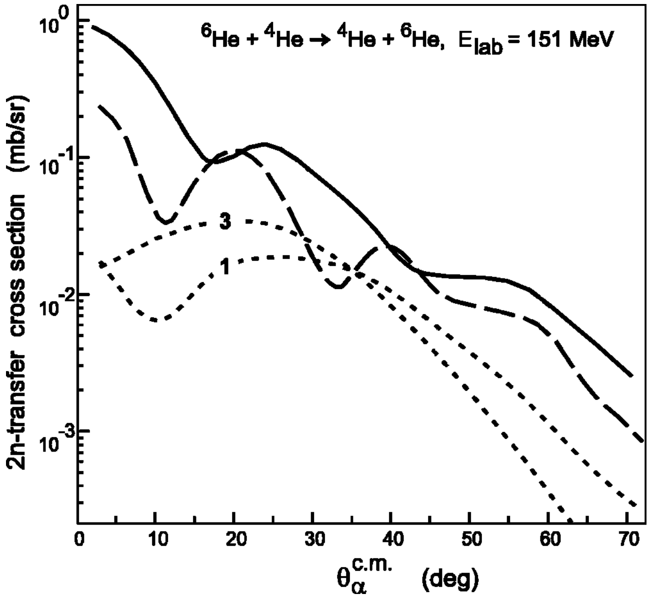

FIG. 12. Contributions of the focusing regions 1 and 3 (see Fig. 11) to the $^4He(^6He,^4He)^6He$(g.s.) two-neutron transfer reaction at $E_{\mathrm{lab}}=151$ MeV are shown by dotted curves 1 and 3 correspondingly. The dashed curve shows the cross section obtained in the limit of strong absorption, i.e., with the ''black'' shadow in regions 1 and 3 (see the text), whereas the solid line shows the total cross section obtained with OMP parameters from the Table I, set 2.

First of all we made the so-called ''near-far'' decomposition of the transition amplitude, integrating in Eq. (14) separately over the ''upper hemisphere'' of the space and over the ''lower hemisphere'' defined relative to the direction of the outgoing particle $\mathbf{k}_f$, see Fig. 11. From a classical trajectory point of view the processes happening in the ''upper hemisphere'' are caused mainly by the trajectories deflected to the positive direction in entrance or exit channels (''near'' part of the outgoing wave), and those in the ''lower hemisphere'' are due to the trajectories deflected to the negative angles (''far'' part of the amplitude). Of course, for the angle $\theta_f=0^\circ$ these parts are equal. With increasing angle θ_f the ''near'' and ''far'' parts of the amplitude behave differently depending mainly on the interactions of the nuclei in entrance and exit channels.

In our case the repulsive part of the interaction between ^6He and ^4He is very small and can give a deflection to positive angles of no more than 1°—see the deflection function in Fig. 10. So, the near part of the transition amplitude

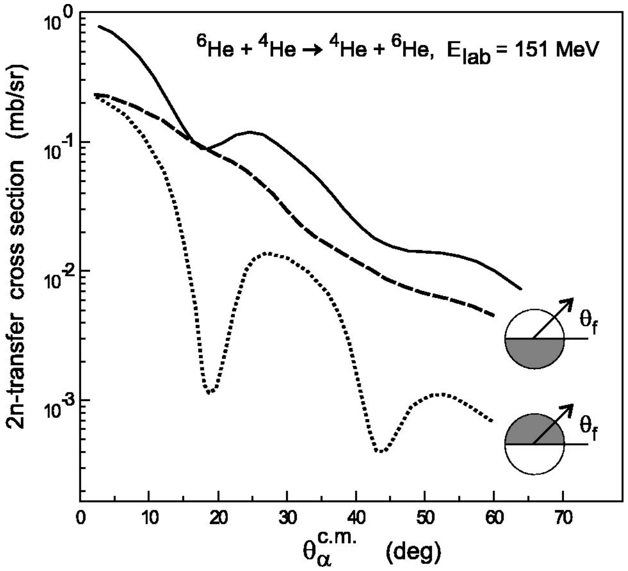

FIG. 13. Spatial localization of the ^{4}He(^{6}He,^{4}He)^{6}He(g.s.) two-neutron transfer reaction at $E_{lab}=151$ MeV. The dashed curve is the contribution to the cross section coming from the ''lower hemisphere'' (relative to the positive outgoing angle θ_f, see the insets), and the dotted curve shows the contribution of the ''upper hemisphere.'' The solid curve corresponds to integration over the whole space.

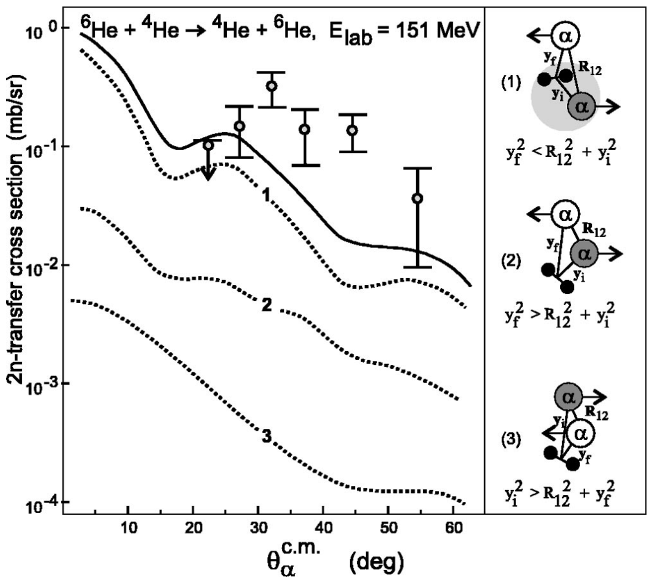

FIG. 14. Contributions of the different spatial configurations of the four-body system to the cross section of the ^{4}He(^{6}He,^{4}He)^{6}He (g.s.) two-neutron transfer reaction at $E_{lab}=151$ MeV. Curves 1–3 correspond to the different configurations (shown in inset) of two α particles and two neutrons during the transfer process.

(i.e., the contribution of the upper hemisphere) is caused mainly by quantum effects, i.e., by diffractive trajectories and has to decrease faster than the ''far'' part of the amplitude, because there are real classical trajectories going to the negative direction up to the nuclear rainbow angle $\theta_R^N \approx -47°$. Our calculations presented in Fig. 13, where the contributions of upper and lower hemispheres of the total space are shown, confirm this suggestion. The dominant contribution to the $2n$-transfer process in the ^{4}He(^{6}He,^{4}He)^{6}He reaction comes from region 2 of Fig. 11 due to the dominant role of the attractive interaction of ^{6}He and ^{4}He.

Direct calculation of the six-dimensional integral (14) allows us to obtain even more interesting information about preferable configurations of the four-body system (see Fig. 1) to the $2n$-transfer reaction. Selection of a definite configuration can be easily done by inserting an additional condition into the multidimensional integral. If we fix, for example, the condition $y_i^2 > R_{12}^2 + y_f^2$ then we choose the configurations where the $2n$-center of mass and the α-particle core of ^{6}He are located on opposite sides of the target, see Fig. 1 and case 3 in Fig. 14. Due to the long tail of the ^{6}He wave function in the channel $2n+{}^4$He we could suppose that quite unusual configurations of the total system can contribute to the $2n$-transfer reaction. However, we found that just the expected configuration of the system, where the transferred neutrons are located between two heavy cores, dominates in the $2n$-transfer reaction (Fig. 14).

4. Dependence on OM potentials

As mentioned above, the present experimental information is insufficient to fix unambiguously the parameters of OM potential for the ^{6}He+^{4}He elastic scattering. The available experimental data at 25 MeV/nucleon [4] (see Fig. 7) allows us to conclude that this potential can be taken from the same potential family (depth-radius) as for the ^{6}Li+^{4}He elastic scattering (Table I) but within the same potential family we need to adjust the parameters of OMP to fit elastic scattering in a wide angular region. The cross section measured in the rather narrow angular region of 17°−59° (Fig. 7) can be fitted more or less accurately with different OMP parameters, in particular, with the two sets (2 and 3) of Table I.

It is well known that transfer reaction cross sections are sensitive to the OMP parameters which are used to calculate the distorted waves entering the DWBA transition amplitude. Changing these parameters we can change the $2n$-transfer cross section by a factor 2 or 3 (Fig. 15). Of course, playing with these parameters within reasonable intervals, we could also obtain much better agreement between calculated and experimental $2n$-transfer cross sections. This is not very meaningful because both the experimental data on elastic scattering and on $2n$-transfer reaction in the ^{6}He+^{4}He collisions are measured within narrow angular regions and with an angular resolution of about ±3°. We hope that in the near future new experimental data on the ^{6}He+^{4}He scattering will be obtained to eliminate some ambiguities in their interpretation. Note that experimental data on elastic scattering of ^{6}He+^{4}He at several different energies (measured in a wide angular region) are desirable to fix finally the OMP parameters for these nuclei.

IV. THE ^{6}He+^{1}H→^{4}He+^{3}H REACTION

A hydrogen target may be the most preferable for studying the structure and spatial configurations of exotic nuclei at

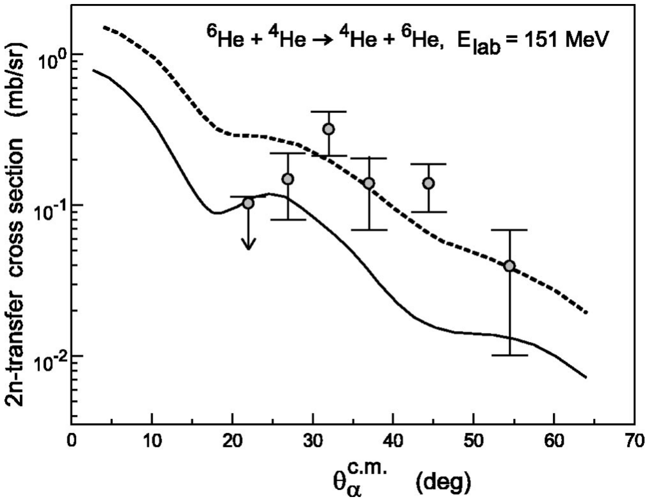

FIG. 15. Dependence of the $2n$-transfer cross section on the optical-model parameters. The solid curve was calculated with the OMP parameters of set 2 of the Table I, whereas the dashed curve was calculated with the parameters of set 3.

medium energies. In this case transfer reaction channels are easily distinguished from elastic scattering. The short range of the proton-neutron interaction and sufficiently small radius of ^{3}H should lead to an enhanced selectivity of transfer reactions to the two spatial configurations in ^{6}He (the dineutron and cigarlike). We may expect, for example, that in peripheral collisions only closely located neutrons in ^{6}He could be captured by the proton (with formation of ^{3}H in its g.s.) with a large probability. Simultaneous measurement of $1n$ transfer cross sections in this reaction gives additional information on collision dynamics and on the structure of ^{6}He.

However, some difficulties arise in the theoretical analysis of the ^{1}H(^{6}He,^{4}He)^{3}H reaction. The Q value is rather large (+7.51 MeV) and can influence considerably the reaction mechanism at low energies. The effective OMP interaction of ^{4}He with ^{3}H in the exit channel is badly determined, but plays an important role in description of the angular distribution of the $2n$ transfer reaction. Finally, the reaction mechanism in a light nuclear system is generally not so simple.

Elastic scattering, one-neutron, and two-neutron transfer cross sections in collisions of ^{6}He with a hydrogen target have been recently measured in Dubna at laboratory energy of 151 MeV [5]. The $2n$ transfer cross sections are shown in Fig. 16 and compared with corresponding data on deuteron transfer in the ^{6}Li(p,^{3}He)^{4}He reaction, obtained previously in [17] at just the same energy.

Three main differences between the two reactions can be seen from the data.

(1) The forward-backward angular asymmetry in the ^{1}H(^{6}He,^{4}He)^{3}H and ^{6}Li(p,^{3}He)^{4}He reactions is opposite. Note, that the dominant yield of ^{3}He at backward angles in the ^{6}Li(p, ^{3}He)^{4}He reaction is mainly due to transfer of ^{3}H from ^{6}Li, whereas the deuteron transfer contributes mainly to the forward angle emission of ^{3}He in this reaction [18]. So, it seems (even without calculation) that ^{3}H+^{3}H clusterization in the ^{6}He g.s. is less probable than the corresponding ^{3}H+^{3}He configuration in ^{6}Li.

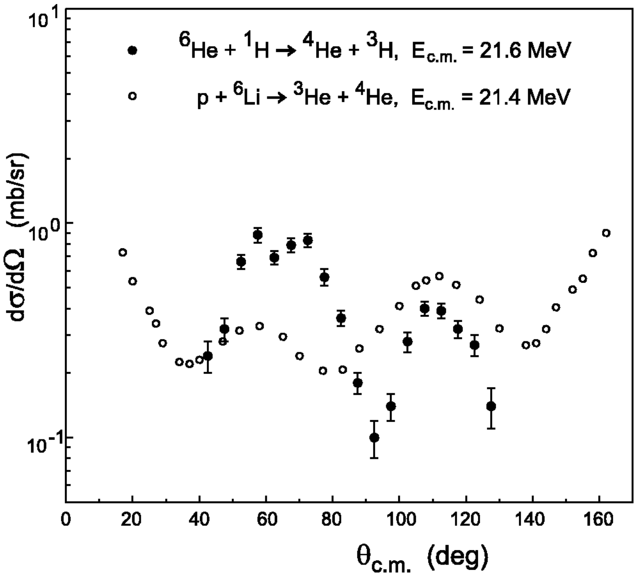

FIG. 16. Experimental data on the $2n$ transfer cross section in the ^{1}H(^{6}He,^{4}He)^{3}H reaction at $E_{c.m.}$=21.6 MeV [5] (solid circles), and on deuteron transfer in the ^{6}Li(p, ^{3}He)^{4}He reaction at $E_{c.m.}$=21.4 MeV [17] (open circles).

(2) The oscillations of the angular distribution in the ^{1}H(^{6}He, ^{4}He)^{3}H reaction are much more pronounced than for ^{6}Li(p, ^{3}He)^{4}He. This may indicate a more ''pure'' reaction mechanism and better l matching (zero angular momentum transfer) in the ^{1}H(^{6}He,^{4}He)^{3}H reaction, because a coherent sum of the contributions coming from different reaction mechanisms and sum over magnetic numbers of transferred angular momentum usually tend to smoothen an interference structure in angular distributions of transfer reactions.

(3) The absolute value of the available $2n$ transfer cross section in the forward hemisphere in the ^{1}H(^{6}He,^{4}He)^{3}H reaction is significantly larger than the deuteron transfer cross section from the ^{6}Li at the same energy of 25 MeV/nucleon. This could be related to more spreading of the $2n$ halo wave function in ^{6}He compared with the more bound deuteron state in ^{6}Li.

A. Elastic scattering of ^{6}He+^{1}H and OM parameters

The problem of elastic scattering of ^{6}He from different target nuclei is very interesting in itself for better understanding of the influence of the halo neutrons on refractive and absorptive properties of the corresponding OM potentials. Polarization effects are expected to be large due to the weakly bound and far extended neutron halo in ^{6}He. Except for very high energies there are, however, only a few experimental data on elastic scattering of ^{6}He from hydrogen target, measured at the energies of 41.6 [19] and 71 [20] MeV/nucleon. In both cases the angular distribution was measured only in the region of forward angles (10°–50° in the center-of-mass system) and can hardly be used for fitting the OM parameters. New data on the ^{6}He+^{1}H elastic scattering at 25 MeV/nucleon were obtained in Dubna [5] in a sufficiently

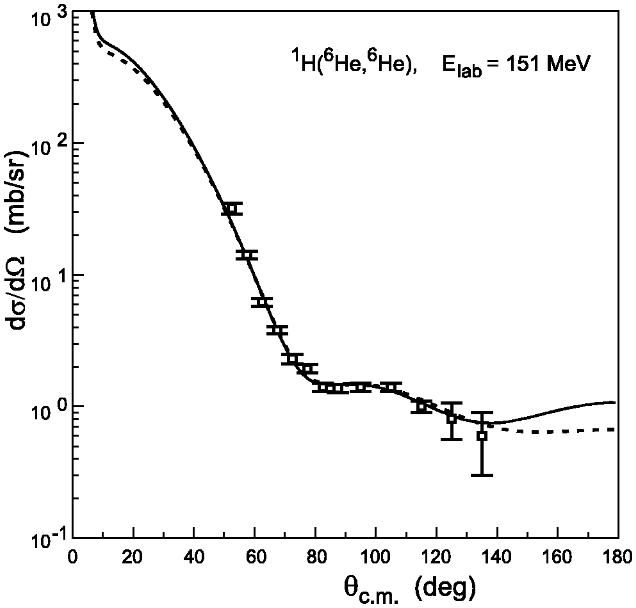

FIG. 17. Elastic scattering of ^{6}He on hydrogen target at E/A $=25.2$ MeV. Solid and dashed curves show the best fits within OM (set 1 and 2 of Table II respectively). Experimental data are from [5].

wide angular range shown in Fig. 17, and allows us to adjust more or less accurately the corresponding OM potential.

Fitting the data we started from two initial sets of OM parameters: the OM parameters obtained for the ^{6}Li$+p$ scattering system at the same energy [22] and the so-called global nucleon-nucleus OM parametrization CH89 [21]. As a result, we found two sets of OM parameters, listed in Table II, which describe the available data on the ^{6}He$+^1$H elastic scattering with equal accuracy. Nevertheless, new data on the ^{6}He$+^1$H elastic scattering in a wider angular range and at several beam energies are quite desirable to make a final conclusion about OMP for this system. Set 1 of Table II is used below to generate the distorted wave $\chi_{\mathbf{k}_i}^{(+)}(\mathbf{R}_i)$ in the entrance channel of the $2n$ transfer reaction ^{1}H(^{6}He,^{4}He)^{3}H.

B. OM potential for ^{4}He+^{3}H

Unfortunately, the situation with elastic scattering of nuclei like ^{3}H or ^{3}He from ^{4}He at lower energies turns out to be less clear than might have been expected after many years of studying these nuclei. We cannot find data on elastic scattering of tritons from α particles, at center-of-mass energies around 30 MeV, and only a few sources on ^{3}He$+^4$He elastic scattering. Thus, OM parameters for these systems are also badly determined. Note, also, that many attempts to fit the experimental data on the ^{3}He$+^4$He elastic scattering at low energies within standard OM calculations were unsuccessful (see, for example, [23]). An agreement as good as for nucleon-nucleus elastic scattering or for ^{3}H(^{3}He) elastic scattering from heavy nuclei was not achieved. Moreover, it was found that only OM potentials with unusually small diffuseness of their real parts could account for essential features of the observed angular distributions in these light systems [24,25].

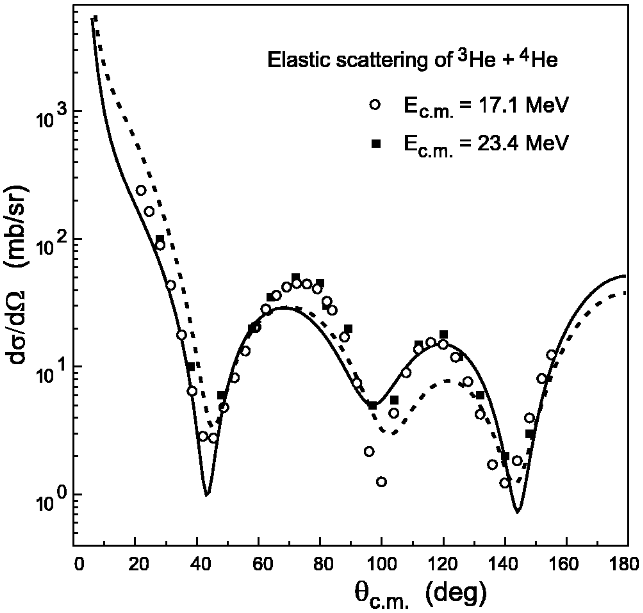

FIG. 18. Elastic scattering of ^{3}He$+^4$He at $E_{\mathrm{c.m.}}=17.1$ MeV [26] (open circles and dashed curve) and 23.4 MeV [27] (solid rectangles and solid curve).

We repeated the fitting of OM parameters using experimental data on elastic scattering of ^{3}He$+^4$He at center-of-mass energies of 17 MeV [26] and 23.4 MeV [27], which were not fitted previously within the standard optical model, see Fig. 18. As usual, we found a discrete and continuous ambiguity in the depth-radius values and fixed the depth of the real part to $V_0=-130$ MeV for both energies. We did not succeed in describing accurately the experimental data, but the best agreement was again achieved only with a very small diffuseness of the real part and with a large radius of the imaginary part of the OM potential. OM parameters found in this way are listed in Table III (sets 1 and 2), whereas set 3 is taken from [24]. The small diffuseness of the real part of the OM potential means a large refractive ability leading to a large cross section at backward angles and to a strong interference in angular distributions, which, in fact, can be due to some exchange process. Strong angular mo-

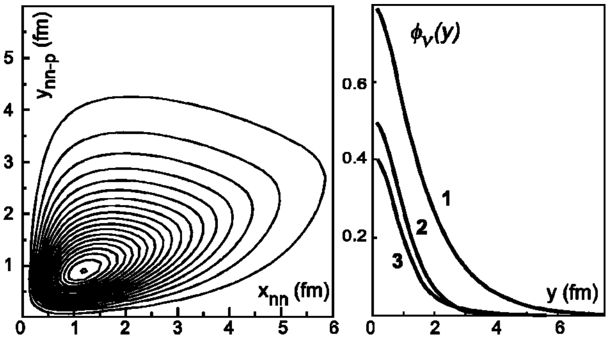

FIG. 19. Spatial correlation density plot (left) and the components of the ^{3}H ground-state wave function corresponding to the relative motion of the two-neutron pair and the proton, see Eq. (23). The curves 1–3 correspond to the states with quantum numbers $Nl_xS=(000)$, (200), and (400).

TABLE II. Optical-model parameters for the ^{6}He+^{1}H elastic scattering at 151 MeV beam energy.

Set	V_{vol} (MeV)	R_V (fm)	a_V (fm)	W_{vol}^{a} (MeV)	R_W^{a} (fm)	a_W^{a} (fm)	W_{surf} (MeV)	R_W (fm)	a_W (fm)	V_{so}^{a} (MeV)	R_{so}^{a} (fm)	a_{so}^{a} (fm)
1	−40.7	2.11	0.573				−3.81	2.80	0.931			
2	−45.4	1.80	0.612	−2.6	2.00	0.690	−3.47	3.20	0.772	−5.9	1.23	0.630

[a] These parameters correspond to the global nucleon-nucleus OMP parametrization CH89 [21] and were fixed during the fit process.

mentum dependence of the effective interaction (not included in standard OM potential) can also lead to unusual behavior of elastic scattering, because in light systems at energies up to several tens of MeV/nucleon only a few partial waves define completely the angular distribution of an elastic cross section.

C. Three-body wave function of ^{3}H ground state

To describe the two-nucleon transfer reactions within our four-body approach, we need also to calculate a three-body bound state wave function of the ^{3}H g.s. formed in the exit channel. This wave function is not of our main interest (in contrast to the ^{6}He wave function) and was supposed to have a simple Jastrow form [28,29] for the radial part (see notation of coordinates in Fig. 1)

$$\Psi^{(134)}_{^{3}\mathrm{H}}(\mathbf{x},\mathbf{y})=A\cdot g_{nn}(x)\cdot g_{pn}(\mathbf{y}-\mathbf{x}/2)\cdot g_{pn}(\mathbf{y}+\mathbf{x}/2)\cdot X^{nn}_{S=0}\cdot \chi^{p}_{1/2}(\sigma), \tag{21}$$

where $g_i(z)=(e^{-\alpha_i z}-e^{-\beta_i z})/\sqrt{z}$, $\chi^{p}_{1/2}$ is the proton spin function, and A is a normalizing coefficient. The short- and long-range parameters α_i and β_i are chosen to reproduce an appropriate asymptotic behavior of the wave function and a realistic radius of the ^{3}H nucleus: $\alpha_{pn}=\sqrt{\frac{1}{3}(m/\hbar^2)\,E^{\mathrm{sep}}_{p}(^{3}\mathrm{H})}$, $\alpha_{nn}=2\sqrt{\frac{1}{3}(m/\hbar^2)\,E^{\mathrm{sep}}_{n}(^{3}\mathrm{H})}-\alpha_{pn}$, where m is the nucleon mass. This gives $\Psi^{(134)}_{^{3}\mathrm{H}}$ (x fixed,$y\to\infty$)$\sim\exp(-\sqrt{(2\mu/\hbar^2)\,E^{\mathrm{sep}}_{p}}y)/y$ and $\Psi^{(134)}_{^{3}\mathrm{H}}(x\to\infty,y=x/2)\sim\exp(-\sqrt{(2\mu/\hbar^2)\,E^{\mathrm{sep}}_{n}}x)/x$, where $\mu=\frac{2}{3}m$. The quantities α_{pn} and α_{nn} are not identical and, thus, the wave function $\Psi^{(134)}_{^{3}\mathrm{H}}$ is not symmetrical in the interchange of proton and neutron, but, in fact, $\alpha_{pn}\approx\alpha_{nn}$ and such asymmetry is very small and cannot noticeably influence the transition amplitude.

The long-range parameters β_i are chosen in accordance with the rms matter radius of ^{3}H, i.e., $\langle R^2\rangle_{^{3}\mathrm{H}}=\frac{1}{3}\langle\Psi^{(134)}_{^{3}\mathrm{H}}|\Sigma^{3}_{i=1}\mathbf{r}^2_i|\Psi^{(134)}_{^{3}\mathrm{H}}\rangle=\frac{1}{3}\langle\Psi^{(134)}_{^{3}\mathrm{H}}|\frac{1}{2}\mathbf{x}^2+\frac{2}{3}\mathbf{y}^2|\Psi^{(134)}_{^{3}\mathrm{H}}\rangle$, where $\mathbf{r}_i$ are the triton c.m. nucleon coordinates, i.e., $\mathbf{r}_1+\mathbf{r}_2+\mathbf{r}_3=0$. We found that the values $\beta_{pn}=\beta_{nn}=4.4$ fm satisfy this condition giving an rms matter radius $\langle R\rangle_{^{3}\mathrm{H}}\approx1.56$ fm. As in the case of ^{6}He (see Sec. II E) the ^{3}H bound-state wave function can be decomposed over the complete set of the two neutron relative motion wave functions (10), giving the same decomposition (11), but with much simpler angular momentum coupling ($S=L=l_x=0$) and with the following resulting functions for the relative motion of the proton and the two neutrons:

$$\Phi^{1/2,\sigma}_{N,l_x=0,S=0}(\mathbf{y})=\phi_{Nl_x=0}(y)\,Y_{00}(\hat{\mathbf{y}})\cdot\chi^{p}_{1/2}(\sigma), \tag{22}$$

$$\phi_{N,l_x=0,S=0}(y)=(A/\sqrt{4\pi})\times\int f_{Nl_{x=0}}(x)\cdot g_{nn}(x)\cdot g_{pn}(\mathbf{y}-\mathbf{x}/2)\cdot g_{pn}(\mathbf{y}+\mathbf{x}/2)\,d^3\mathbf{x}. \tag{23}$$

The correlation density plot for the ground state of ^{3}H calculated in accordance with Eq. (9) and the functions $\phi_{Nl_x}(y)$ are shown in Fig. 19 and can be compared with the corresponding components of the ^{6}He bound state shown in Fig. 12. For ^{3}H the $1s$ state of p-$2n$ relative motion is, as expected, the dominant component.

D. Dineutron transfer

Using the prior form of the DWBA transition amplitude (5), three-body ground-state wave functions of ^{6}He (7) and ^{3}H (21), and three-dimensional distorted waves generated by OM potentials with parameters from Table II, set 1 (entrance channel) and Table III, set 1 (exit channel), we calculated the differential cross section of the $2n$ transfer reaction ^{1}H(^{6}He,^{4}He)^{3}H shown in Fig. 20. We used a proton-neutron interaction $V_{13}=V_{14}$ of Gaussian shape with -45 MeV depth and 1.7 fm width, and a proton-α interaction V_{12} of Woods-Saxon shape with parameters $V_0=-43$ MeV, $R=1.984$ fm, and $a=0.25$ fm proposed in [30].

TABLE III. Optical-model parameters for the ^{3}He+^{4}He elastic scattering.

Set	$E_{\mathrm{c.m.}}$ (MeV)	V_{vol} (MeV)	R_V (fm)	a_V (fm)	W_{vol} (MeV)	R_W (fm)	a_W (fm)	V_{so} (MeV)	R_{so} (fm)	a_{so} (fm)
1	23.4	−130	1.64	0.217	−1.8	2.1	0.700			
2	17.1	−130	2.58	0.177	−1.6	5.4	0.800			
3	18.0	−173	2.28	0.145	−1.1	5.3	1.050	−1.0	2.28	0.145

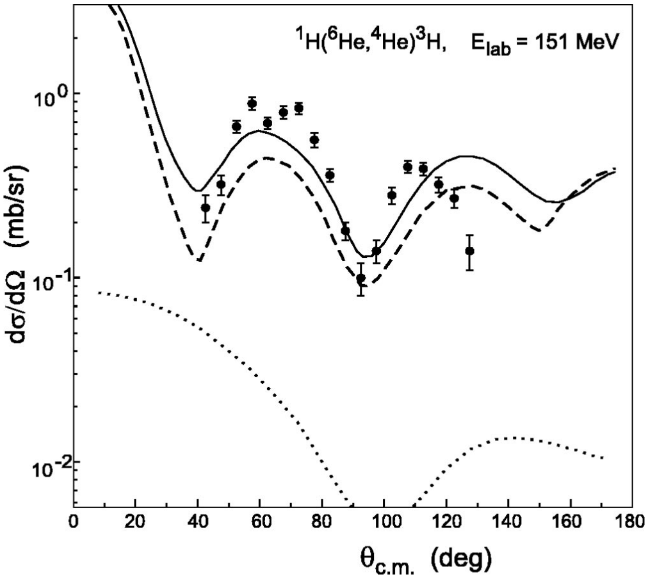

FIG. 20. Cross section of the $2n$ transfer reaction ^{1}H(^{6}He,^{4}He)^{3}H at $E_{\mathrm{c.m.}}=21.4\,\mathrm{MeV}$ [5]. The calculated cross section is shown by the solid line, whereas the dashed and dotted lines show the contributions of the dineutron and cigarlike configurations of ^{6}He to the process.

Favorable agreement with the experimental data (both in absolute value and angular distribution) makes us conclude again that the three-body model wave function (7) describes adequately the ground state of ^{6}He and that the spectroscopic amplitude of the three-body configuration is close to unity. As was expected, the probability for a proton to pickup two neutrons from ^{6}He with formation of the ^{3}H nucleus is much greater in the case when these two neutrons are located close to each other. This leads to striking dominance of the dineutron configuration of ^{6}He in the $2n$ transfer reaction ^{1}H(^{6}He,^{4}He)^{3}H as seen in Fig. 20. In contrast with the ^{4}He(^{6}He,^{4}He)^{6}He reaction, the cigarlike configuration of ^{6}He makes here a negligible contribution to the $2n$ transfer reaction in the whole angular region.

Like in Sec. III B 3, here we also looked for which four-body spatial configurations $(p+\alpha+2n)$ bring the main contributions to the cross section of the $2n$ transfer reaction ^{1}H(^{6}He,^{4}He)^{3}H. Comparing with the ^{6}He+^{4}He collision (Fig. 14) we found that though the configuration α-$2n$-p (see the corresponding case 1 in Fig. 14) regulates the $2n$ transfer cross section, the configuration α-p-$2n$ (where the proton moves very close to the α core in central collisions) also makes a noticeable contribution to the reaction at backward angles.

Note, finally, that the optical model potential in the exit channel (^{3}H+^{4}He) is the most uncertain quantity in our calculations of the ^{1}H(^{6}He,^{4}He)^{3}H transfer reaction cross section. It is expected that OM potentials of ^{3}He and ^{3}H ought to be close to each other. We found that only those OM potentials which describe rather well the angular distributions of elastic scattering of ^{3}He+^{4}He (see Table III and Fig. 18), give simultaneously a reasonable agreement with the cross section of the two-neutron transfer reaction. In spite of some differences, the transfer cross sections, calculated with the different OM potentials of ^{3}H+^{4}He, have similar angular behavior and close absolute values. It means that our main conclusions about reaction dynamics obtained above are quite reliable. However, experimental data on the ^{3}H+^{4}He elastic scattering at c.m. energies of about 30 MeV/nucleon are desirable for eliminating present uncertainties and for better understanding of the main reasons for the difference between the calculated and experimental two-neutron transfer cross sections. In particular, the transfer cross section at forward angles (not measured yet experimentally) was found to be very sensitive to the imaginary part of the OM potential in the exit channel, decreasing with increasing $W^{\mathrm{OM}}(^3\mathrm{H}+^4\mathrm{He})$.

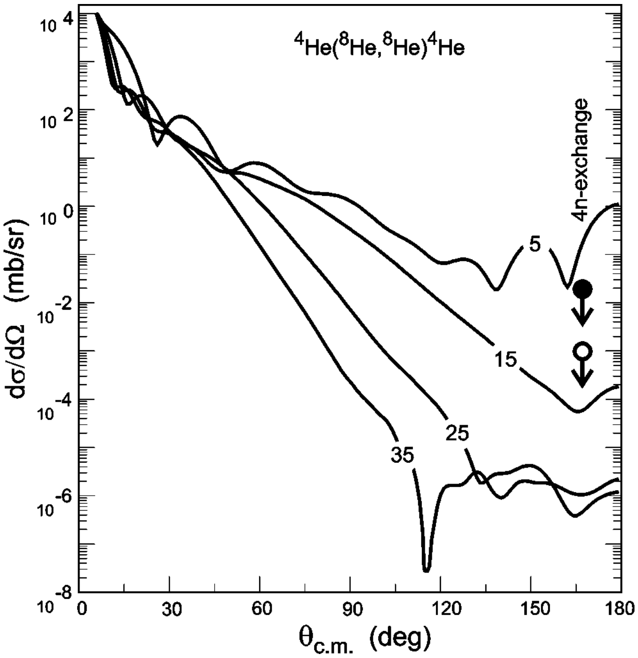

FIG. 21. Potential elastic scattering of ^{8}He from ^{4}He at different incident energies (curves) and estimated upper limits of the $4n$ exchange contribution to the elastic scattering at backward angles at $E/A=20\,\mathrm{MeV}$ (solid circle), and 30 MeV (open circle).

V. THE ^{8}He+^{4}He COLLISION

The structure of ^{8}He is more complicated and is less understood than that of ^{6}He. The multineutron transfer reactions could help us to understand better the dominant configurations of this nucleus. In particular, the measurements of $1n$, $2n$, $3n$, and $4n$-transfer reaction cross sections with subsequent analysis within a few-body model would supply us with direct information on spectroscopy of the (^{4}He$+^3n+^1n$), (^{4}He$+^2n+^2n$), (^{6}He$+^2n$), and (^{4}He$+^4n$) configurations in ^{8}He. All these transfer reactions should be performed with accurate selection of exit channels, i.e., in coincident experiments, to distinguish the two-body primary reaction channels from the others. Incident energies should not be too high, to allow us to measure the cross sections of multineutron transfer reactions at low intensity secondary beam of ^{8}He.

Preliminary estimations of the ^{8}He+^{4}He elastic scattering cross sections are shown in Fig. 21 for the energy interval of 5–35 MeV/nucleon. The upper limits of the tetraneutron transfer cross sections (manifested in elastic scattering at backward angles due to symmetry of the entrance and exit channels) calculated at energies $E/A=20$ and 30 MeV are also shown in this figure. From these results we may conclude the following: (i) The $4n$-transfer reaction cross section in the ^{8}He+^{4}He collisions can be easily distinguished from potential scattering at energies of about 20 MeV/nucleon and higher. (ii) With increasing beam energy the $4n$-transfer reaction cross section decreases (one order of magnitude with each 10*A* MeV). (iii) At beam energies lower than 10 MeV/nucleon the $4n$-exchange process cannot be easily separated from potential scattering at backward angles. It means that some other target has to be chosen to study this process at low energies.

Comparing the absolute values of the $4n$ and $2n$ transfer cross sections (with formation of two ^{6}He nuclei in the exit channel in the last case), we are already able to conclude about the dominant valence neutron configuration in ^{8}He. The first experiments of this type are now being prepared at FLNR (Dubna).

VI. SUMMARY

A new four-body three-dimensional DWBA approach has been developed for the description of two-nucleon transfer reactions $1+[2(34)]\rightarrow[1(34)]+2$, in which the three-body nature (core+two valence nucleons) of the bound-state wave functions of projectile and ejectile are the main subjects of investigation. By focusing on the spatial localization of distorted waves as well as bound states, the $2n$-transfer process in collisions of ^{6}He with ^{4}He and hydrogen targets has been analyzed in detail, testing the three-body structure of the Borromean nucleus ^{6}He against available experimental data as on elastic scattering of ^{6}He from ^{4}He and ^{1}H and on $2n$ transfer cross sections at $E/A=25$ MeV.

Although the angular range and statistics of the data should be improved, comparison of calculated and experimental cross sections for the two reactions and analysis of the $2n$ transfer reaction dynamics argue for the following conclusions. (i) A predominant three-body $n-n-\alpha$ configuration of ^{6}He is consistent with the data, justifying the label Borromean, i.e., the spectroscopic factor $S_{(2n)\alpha}(^6\text{He})\approx 1$. (ii) The spatial dineutron component of this three-body configuration dominates in $2n$ transfer reactions induced by ^{6}He at energies higher than 10 MeV/nucleon. This dominance is especially striking in the case of a hydrogen target. (iii) ^{3}H+^{3}H clusterization in ^{6}He seems to be much less probable compared with the ^{3}H+^{3}He configuration of ^{6}Li. Although our consistent DWBA studies compare well with available data, there are noticeable deviations concerning details. A substantial sensitivity to optical potentials is also present. Thus it is of interest to investigate channel couplings involving the low-lying ^{6}He continuum. Work to this end is in progress, with form factors based on three-body continuum states as well as the ground state of ^{6}He.

We have also via preliminary estimates indicated that experiments on $4n$ and $2n$ transfer reactions at beam energies of 10–30 MeV/nucleon could be very useful for probing the five-body structure of the extremely neutron-rich double-Borromean ^{8}He nucleus.

ACKNOWLEDGMENTS

The authors thank B. V. Danilin, S. N. Ershov, K. A. Gridnev, and M. V. Zhukov for illuminating discussions.

---

[1] M. V. Zhukov, B. V. Danilin, D. V. Fedorov, J. M. Bang, I. J. Thompson, and J. S. Vaagen, Phys. Rep. **231**, 151 (1993).
[2] I. Tanihata, J. Phys. G **22**, 157 (1996).
[3] M. J. G. Borge, L. Johannsen, B. Jonson, T. Nilson, G. Nyman, K. Riisager, O. Tengblad, and K. Wilhelmsen Rolander, Nucl. Phys. **A560**, 663 (1993).
[4] G. M. Ter-Akopian, A. M. Rodin, A. S. Fomichev, S. I. Sidorchuk, S. V. Stepantsov, R. Wolski, M. L. Chelnokov, V. A. Gorshkov, A. Yu. Lavrentev, V. I. Zagrebaev, and Yu. Ts. Oganessian, Phys. Lett. B **426**, 251 (1998).
[5] R. Wolski, A. S. Fomichev, A. M. Rodin, S. I. Sidorchuk, S. V. Stepantsov, G. M. Ter-Akopian, M. L. Chelnokov, V. A. Gorshkov, A. Yu. Lavrentev, V. I. Zagrebaev, Yu. Ts. Oganessian, P. Roussel-Chomaz, W. Mittig, and I. David, JINR Report No. E15-98-284, Dubna, 1998.
[6] V. Zagrebaev, A. Kozhin, Nuclear Reaction Video (knowledge base on low-energy nuclear physics), Optical Model, JINR report No. E10-99-151, Dubna, 1999, http://nrv.jinr.ru/nrv/
[7] V. I. Zagrebaev, Ann. Phys. (N.Y.) **197**, 33 (1990).
[8] B. V. Danilin, M. V. Zhukov, A. A. Korsheninnikov, and L. V. Chulkov, Yad. Fiz. **53**, 71 (1991) [Sov. J. Nucl. Phys. **53**, 45 (1991)].
[9] B. V. Danilin, I. J. Thompson, M. V. Zhukov, and J. S. Vaagen, Nucl. Phys. **A632**, 383 (1998).
[10] R. J. Ascuitto and E. A. Seglie, in *Treatise on Heavy-Ion Science*, edited by D. A. Bromley (Plenum, New York, 1984), Vol. 1, p. 463.
[11] G. R. Satchler, *Direct Nuclear Reactions* (Clarendon, Oxford, 1983).
[12] D. Bachelier, M. Bernas, J. L. Boyard, H. L. Harney, J. C. Jourdain, P. Radvanyi, M. Roy-Stephan, and R. Devries, Nucl. Phys. **A195**, 361 (1972).
[13] A. M. Rodin, S. I. Sidorchuk, S. V. Stepantsov, G. M. Ter-Akopian, R. Wolski, V. B. Galinskiy, G. V. Ivanov, I. B. Ivanova, V. A. Gorshkov, A. Yu. Lavrentev, and Yu. Ts. Oganessian, Nucl. Instrum. Methods Phys. Res. B **126**, 236 (1997).
[14] D. Baye, L. Desorgher, D. Guillain, and D. Herschkowitz, Phys. Rev. C **54**, 2563 (1996).
[15] Y. Suzuki and K. Ikeda, Phys. Rev. C **38**, 410 (1988).
[16] Y. Suzuki, Nucl. Phys. **A528**, 395 (1991).

[17] K. Schenk, M. Mörike, G. Staudt, P. Turek, and D. Clement, Phys. Lett. B **52**, 36 (1974).
[18] M. F. Werby, M. B. Greenfield, K. W. Kemper, D. L. McShan, and S. Edwards, Phys. Rev. C **6**, 106 (1973).
[19] M. D. Cortina-Gil, P. Roussel-Chpmaz, N. Alamanos, J. Barrette, W. Mittig, F. Auger, Y. Blumenfeld, J. M. Casandjian, M. Chartier, V. Fekou-Youmbi, B. Fernandez, N. Frascaria, A. Gillibert, H. Laurent, A. Lepine-Szily, N. A. Orr, V. Pascalon, J. A. Scarpaci, J. L. Sida, and T. Suomijarvi, Phys. Lett. B **371**, 14 (1996).
[20] A. A. Korsheninnikov, S. Fukuda, T. Kobayashi, S. Momota, A. Ozawa, I. Tanihata, K. Yoshida, O. V. Bochkarev, E. A. Kuzmin, E. Yu. Nikolskii, B. G. Novatskii, A. A. Ogloblin, and V. Probora, in *Proceedings on Physics of Unstable Nuclear Beams*, Serra Negra, Brazil, 1996, edited by C. A. Bertulani, L. F. Canto, and M. S. Hussein (World Scientific, Singapore 1996), p. 86.
[21] R. L. Varner, W. J. Thompson, T. L. McAbee, E. J. Ludwig, and T. B. Clegg, Phys. Rep. **201**, 57 (1991).
[22] K. H. Bray, M. Jain, K. S. Jayaraman, G. Lobianco, G. A. Moss, W. T. H. Van Oers, and D. O. Wells, Nucl. Phys. **A189**, 35 (1972).
[23] F. Dunnil, T. J. Gray, H. T. Fortune, and N. R. Fletcher, Nucl. Phys. **A93**, 201 (1967).
[24] J. S. Vincent and E. T. Boschitz, Nucl. Phys. **A143**, 121 (1970).
[25] R. P. Ward and P. R. Hayes, At. Data Nucl. Data Tables **49**, 315 (1991).
[26] C. G. Jacobs, Jr. and R. E. Brown, Phys. Rev. C **1**, 1615 (1970).
[27] R. Chiba, H. E. Conzett, H. Morinaga, N. Mutsuro, K. Shoda, and M. Kimura, J. Phys. Soc. Jpn. **16**, 1077 (1961).
[28] R. Jastrow, Phys. Rev. **98**, 1479 (1955).
[29] J. N. Pappademos, Nucl. Phys. **42**, 122 (1963).
[30] G. R. Satchler, L. W. Owen, A. J. Elwyn, G. L. Morgan, and R. L. Walter, Nucl. Phys. **A112**, 1 (1968).